

# The JCMT Nearby Galaxies Legacy Survey III: Comparisons of cold dust, polycyclic aromatic hydrocarbons, molecular gas, and atomic gas in NGC 2403

G. J. Bendo<sup>1</sup>, C. D. Wilson<sup>2</sup>, B. E. Warren<sup>2,3</sup>, E. Brinks<sup>4</sup>, H. M. Butner<sup>5</sup>, P. Chanial<sup>1,6</sup>, D. L. Clements<sup>1</sup>, S. Courteau<sup>7</sup>, J. Irwin<sup>7</sup>, F. P. Israel<sup>8</sup>, J. H. Knapen<sup>9,10</sup>, J. Leech<sup>11</sup>, H. E. Matthews<sup>12</sup>, S. Mühle<sup>13</sup>, G. Petitpas<sup>14</sup>, S. Serjeant<sup>15</sup>, B. K. Tan<sup>11</sup>, R. P. J. Tilanus<sup>16,17</sup>, A. Usero<sup>4,18</sup>, M. Vaccari<sup>19</sup>, P. van der Werf<sup>8</sup>, C. Vlahakis<sup>8</sup>, T. Wiegert<sup>20</sup>, M. Zhu<sup>12,16</sup>

<sup>1</sup>*Astrophysics Group, Imperial College, Blackett Laboratory, Prince Consort Road, London SW7 2AZ, United Kingdom*

<sup>2</sup>*Department of Physics & Astronomy, McMaster University, Hamilton, Ontario L8S 4M1, Canada*

<sup>3</sup>*ICRAR, M468, University of Western Australia, Crawley, WA, 6009, Australia*

<sup>4</sup>*Centre for Astrophysics Research, University of Hertfordshire, College Lane, Hatfield AL10 9AB, United Kingdom*

<sup>5</sup>*Department of Physics and Astronomy, James Madison University, 911 Carrier Drive, Harrisonburg, VA 22807, USA*

<sup>6</sup>*Laboratoire AIM, CEA/DSM - CNRS - Universit Paris Diderot, Irfu/SAP, 91191 Gif-sur-Yvette, France*

<sup>7</sup>*Department of Physics, Engineering Physics and Astronomy, Queen's University, Kingston, Ontario K7L 3N6, Canada*

<sup>8</sup>*Sterrewacht Leiden, Leiden University, PO Box 9513, 2300 RA Leiden, The Netherlands*

<sup>9</sup>*Instituto de Astrofísica de Canarias, E-38200 La Laguna, Tenerife, Spain*

<sup>10</sup>*Departamento de Astrofísica, Universidad de La Laguna, E-38205 La Laguna, Tenerife, Spain*

<sup>11</sup>*Department of Physics, University of Oxford, Keble Road, Oxford OX1 3RH, United Kingdom*

<sup>12</sup>*National Research Council Canada, Herzberg Institute of Astrophysics, DRAO, P.O. Box 248, White Lake Road, Penticton, British Columbia V2A 69J, Canada*

<sup>13</sup>*Joint Institute for VLBI in Europe, Postbus 2, 7990 AA Dwingeloo, The Netherlands*

<sup>14</sup>*Harvard-Smithsonian Center for Astrophysics, 60 Garden St., MS-78, Cambridge, MA 02138, USA*

<sup>15</sup>*Department of Physics & Astronomy, The Open University, Milton Keynes MK7 6AA, United Kingdom*

<sup>16</sup>*Joint Astronomy Centre, 660 N. A'ohoku Pl., University Park, Hilo, HI 96720, USA*

<sup>17</sup>*Netherlands Organisation for Scientific Research, Laan van Nieuw Oost-Indie 300, NL-2509 AC The Hague, The Netherlands*

<sup>18</sup>*Observatorio de Madrid, OAN, Alfonso XII, 3, E-28014 Madrid, Spain*

<sup>19</sup>*Dipartimento di Astronomia, Università di Padova, Vicolo dell'Osservatorio 5, 35122 Padua, Italy*

<sup>20</sup>*Department of Physics and Astronomy, University of Manitoba, Winnipeg, Manitoba R3T 2N2, Canada*

## ABSTRACT

We used 3.6, 8.0, 70, 160  $\mu\text{m}$  *Spitzer* Space Telescope data, James Clerk Maxwell Telescope HARP-B CO  $J=(3-2)$  data, National Radio Astronomy Observatory 12 meter telescope CO  $J=(1-0)$  data, and Very Large Array HI data to investigate the relations among PAHs, cold ( $\sim 20$  K) dust, molecular gas, and atomic gas within NGC 2403, an SABcd galaxy at a distance of 3.13 Mpc. The dust surface density is mainly a function of the total (atomic and molecular) gas surface density and galactocentric radius. The gas-to-dust ratio monotonically increases with radius, varying from  $\sim 100$  in the nucleus to  $\sim 400$  at 5.5 kpc. The slope of the gas-to-dust ratio is close to that of the oxygen abundance, suggesting that metallicity strongly affects the gas-to-dust ratio within this galaxy. The exponential scale length of the radial profile for the CO  $J=(3-2)$  emission is statistically identical to the scale length for the stellar continuum-subtracted 8  $\mu\text{m}$  (PAH 8  $\mu\text{m}$ ) emission. However, CO  $J=(3-2)$  and PAH 8  $\mu\text{m}$  surface brightnesses appear uncorrelated when examining sub-kpc sized regions.

**Key words:** galaxies: individual: NGC 2403, galaxies: ISM, galaxies: spiral, infrared: galaxies, radio lines: galaxies

## 1 INTRODUCTION

The James Clerk Maxwell Telescope (JCMT) Nearby Galaxies Legacy Survey (NGLS) is an 850  $\mu\text{m}$  and CO  $J=(3-2)$  survey

arXiv:0911.3369v1 [astro-ph.CO] 17 Nov 2009

with the goals of studying molecular gas and dust in a representative sample of galaxies within 25 Mpc. The sample contains three subsets: a subset of 31 galaxies from the *Spitzer* Infrared Nearby Galaxies Survey (SINGS; Kennicutt et al. 2003) sample; an HI flux-limited sample of 36 galaxies in the Virgo Cluster; and an HI flux-limited sample of 72 field galaxies. At this point in time, CO  $J=(3-2)$  observations of the SINGS galaxies and Virgo Cluster galaxies have been completed. Aside from the 3.6–160  $\mu\text{m}$  data from SINGS that resolve structures less than a kiloparsec in size in the closest galaxies, HI Nearby Galaxies Survey (THINGS; Walter et al. 2008) are also available for many of these galaxies. Together, these data are a powerful dataset for studying the properties of the interstellar medium (ISM) on sub-kiloparsec scales within nearby galaxies such as variations in gas-to-dust ratios on sub-kiloparsec scales.

Gas-to-dust ratios within nearby galaxies have been a major topic of research since the launch of the Infrared Astronomical Satellite (IRAS). Debate on this subject began when dust masses derived from IRAS 60 and 100  $\mu\text{m}$  data seemed a factor of 10 too low to match what was expected either from the depletion of metals from the ISM or from the ratio of gas column density to dust extinction (e.g. Young et al. 1986, 1989; Devereux & Young 1990). More recent calculations of global gas and dust masses using *Spitzer* Space Telescope (Werner et al. 2004) and James Clerk Maxwell Telescope data for spiral galaxies produce gas-to-dust mass ratios of  $\sim 150$  (e.g. Regan et al. 2004; Bendo et al. 2006; Draine et al. 2007). Although the measured ratios are reliant upon CO to H<sub>2</sub> mass conversion factors that do not vary with metallicity or star formation activity, the ratios that were measured are close to what is expected from the ratio for the Milky Way derived from the comparison of gas column densities to optical extinction (e.g. Krügel 2003; Whittet 2003) or from the depletion of metals from the ISM (e.g. Whittet 2003; Li 2004; Krügel 2008). Therefore, the natural expectation would be that dust emission from kiloparsec-sized regions should be correlated with the sum of atomic and molecular gas emission on those spatial scales. However, since the gas-to-dust ratio depends on metallicity and since metallicity varies with radius within most galaxies (e.g. Vila-Costas & Edmunds 1992; Zaritsky et al. 1994; van Zee et al. 1998), the gas-to-dust ratio should decrease with radius. For the most part, these assumptions are only beginning to be tested, mainly because the combination of HI, CO, and far-infrared dust emission data that is resolved on kiloparsec scales has not been available for nearby galaxies.

Related to this topic is the association between polycyclic aromatic hydrocarbon (PAH) emission in the mid-infrared and other constituents of the cold ISM. Several observational studies using data from either the Infrared Space Observatory (ISO; Kessler et al. 1996) or *Spitzer* have shown that, in nearby spiral galaxies, PAH emission is strongly correlated with cold ( $\sim 20$  K) dust emission in the far-infrared, at least on scales  $\gtrsim 1$  kpc (e.g. Mattila et al. 1999; Haas et al. 2002; Bendo et al. 2006, 2008; Zhu et al. 2008). Additionally, (Regan et al. 2006) found that PAH emission is correlated with CO spectral line emission at submillimetre and millimetre wavelengths within nearby spiral galaxies, although these results are based on using radial averages. These results strongly suggested that PAH emission is a tracer of both dust and gas in the cold interstellar medium (ISM).

Some of the SINGS/THINGS/JCMT NGLS galaxies have already been used in comparisons of HI and CO emission with star formation, including measures of star formation that incorporate 24  $\mu\text{m}$  emission (e.g. Kennicutt et al. 2007; Bigiel et al. 2008; Wilson et al. 2009). These studies have found that star formation

is correlated with molecular gas surface density or with a sum of molecular and atomic gas surface density; no correlation exists between star formation and HI emission by itself. Since 24  $\mu\text{m}$  dust emission is included in these comparisons, the results imply that dust emission should be correlated with molecular or total gas surface densities but not with atomic gas surface densities, although a direct comparison between dust, atomic gas, and molecular gas is needed.

As a first look into these topics with the combined SINGS, THINGS, and JCMT NGLS data, we compare PAH, cold dust, CO  $J=(3-2)$ , and HI on sub-kiloparsec scales for NGC 2403. This SABcd spiral galaxy (de Vaucouleurs et al. 1991) was selected because it is relatively nearby (Freedman et al. 2001, the distance to the galaxy is  $3.13 \pm 0.14$  Mpc; ), the galaxy and the dust emission is very extended (the optical disc is  $21.9$  arcmin  $\times$   $12.3$  arcmin; de Vaucouleurs et al. 1991). While the inclination is  $62.9^\circ$  (de Blok et al. 2008), the galaxy is close enough to face-on that it is possible to distinguish spiral structures and individual star-forming regions. As is found in similar late-type spiral galaxies, the regions with the strongest star formation are located outside the centre of the galaxy (e.g. Drissen et al. 1999; Bendo et al. 2008), while the cold dust emission peaks in the centre (Bendo et al. 2008). Consequently, emission related to star formation can be easily disentangled from emission related to dust surface density.

## 2 OBSERVATIONS AND DATA REDUCTION

### 2.1 Mid-infrared data

We use the 3.6 and 8.0  $\mu\text{m}$  data taken with the Infrared Array Camera (IRAC; Fazio et al. 2004) on *Spitzer* as part of SINGS. The observations consisted of a series of 5 arcmin  $\times$  5 arcmin individual frames taken in a mosaic pattern that covers a 25 arcmin  $\times$  25 arcmin region. The data used for this analysis come from astronomical observation requests (AORs) 5505792 and 5505536, which were separated by four days; these separate observations allow for the identification and removal of transient phenomena, particularly asteroids. The full-width half-maxima (FWHM) of the point spread functions (PSFs), as stated in the *Spitzer* Observer’s Manual (*Spitzer* Science Center 2007)<sup>1</sup>, are 1.7 and 2.0 arcsec at 3.6 and 8.0  $\mu\text{m}$ , respectively. Details on the observations can be found in the documentation for the SINGS fifth data delivery (SINGS Team 2007)<sup>2</sup>.

The final images were created from version 14 of the basic calibrated data frames produced by the *Spitzer* Science Center. The data were then processed through the SINGS IRAC pipeline, which applies distortion and rotation corrections, adjusts the offsets among the data frames, removes cosmic rays, subtracts the background, and then combines them together using a drizzle technique. A description of the technique is presented in Regan et al. (2006) and (SINGS Team 2007). The flux calibration is expected to be accurate to 3% (*Spitzer* Science Center 2007).

The final IRAC images include a residual background with a gradient. We interpolated a smoothed version of the background outside the optical disc of the galaxy to determine the background levels within the optical disc, and we then subtracted this background from the data. We then masked out regions contaminated

<sup>1</sup> <http://ssc.spitzer.caltech.edu/documents/som/>

<sup>2</sup> Available at [http://data.spitzer.caltech.edu/popular/sings/20070410\\_enhanced\\_v1/Documents/sings\\_fifth\\_delivery\\_v2.pdf](http://data.spitzer.caltech.edu/popular/sings/20070410_enhanced_v1/Documents/sings_fifth_delivery_v2.pdf)

by emission from bright foreground stars (identified as unresolved sources in the unconvolved IRAC data with  $3.6\ \mu\text{m}/8\ \mu\text{m}$  surface brightness ratios  $\gtrsim 5$ ). To correct for the diffusion of light through the IRAC detector substrate, the  $3.6\ \mu\text{m}$  and  $8.0\ \mu\text{m}$  data are multiplied by the “infinite” aperture corrections described by Reach et al. (2005), which should not be confused with the types of aperture corrections used for measuring the flux densities of unresolved sources. The correction factors are 0.944 and 0.737 at  $3.6$  and  $8.0\ \mu\text{m}$ , respectively. We then subtracted the stellar continuum from the  $8\ \mu\text{m}$  surface brightness maps (in  $\text{MJy sr}^{-1}$ ) using

$$I_\nu(\text{PAH } 8\mu\text{m}) = I_\nu(8\mu\text{m}) - 0.232I_\nu(3.6\mu\text{m}), \quad (1)$$

which was derived by Helou et al. (2004). We will henceforth refer to this as PAH  $8\ \mu\text{m}$  emission so as to distinguish it from the  $8\ \mu\text{m}$  emission that includes stellar continuum emission.

## 2.2 Far-infrared data

We used the Multiband Imaging Photometer for Spitzer Rieke et al. (MIPS; 2004)  $70$  and  $160\ \mu\text{m}$  data taken of NGC 2403 as part of SINGS. These observations are composed of the AORs 5549568 and 5549824. These AORs are scan map observations of the galaxy that were performed at the medium scan speed. Each scan map is  $\sim 0.5^\circ$  wide and  $1^\circ$  long, which is sufficiently wide to cover the entire optical disc of the galaxy. The two AORs were executed three days apart so as to allow for the identification and removal of transient sources, although most detectable sources usually affect only the  $24\ \mu\text{m}$  band. The FWHM of the PSFs are 18 arcsec at  $70\ \mu\text{m}$  and 38 arcsec at  $160\ \mu\text{m}$  (Spitzer Science Center 2007). The documentation for the SINGS fifth data delivery (SINGS Team 2007) contains additional details on the observing strategy.

The  $70$  and  $160\ \mu\text{m}$  images were created from raw data frames using the MIPS Data Analysis Tools (MIPS DAT; Gordon et al. 2005) version 3.10 along with additional processing steps. First, ramps were fit to the  $70$  and  $160\ \mu\text{m}$  reads to derive slopes. In this step, readout jumps and cosmic ray hits were also removed, and an electronic nonlinearity correction was applied. Next, the stim flash frames (frames of data in which a calibration light source was flashed at the detectors) were used as responsivity corrections. After this, the dark current was subtracted from the data, and an illumination correction was applied. Following this, short term variations in the signal (often referred to as drift) were removed, and additional periodic variations in the background related to the stim flash cycle were subtracted; this also subtracted the background from the data. Next, a robust statistical analysis was applied to cospatial pixels from different frames in which statistical outliers (which could be pixels affected by cosmic rays) were masked out. Once this was done, final mosaics were made using pixel sizes of  $4.5\ \text{arcsec}^2$  for the  $70\ \mu\text{m}$  data and  $9\ \text{arcsec}^2$  for the  $160\ \mu\text{m}$  data. The residual backgrounds in the data were measured in regions outside the optical discs of the galaxies and subtracted, and then flux calibration factors (given as  $702 \pm 35\ \text{MJy sr}^{-1}$  [MIPS instrumental unit] $^{-1}$  for the  $70\ \mu\text{m}$  data by Gordon et al. (2007) and  $41.7 \pm 5\ \text{MJy sr}^{-1}$  [MIPS instrumental unit] $^{-1}$  for the  $160\ \mu\text{m}$  data by Stansberry et al. (2007)) were applied to the data. An additional  $70\ \mu\text{m}$  nonlinearity correction given as

$$f_{70\mu\text{m}}(\text{true}) = 0.581(f_{70\mu\text{m}}(\text{measured}))^{1.13} \quad (2)$$

by Dale et al. (2005) was applied to coarse-scale imaging data where the surface brightness exceeded  $66\ \text{MJy sr}^{-1}$ .

The final  $70\ \mu\text{m}$  image is affected by latent images, which are dark images that appear after the array has observed a bright

source. The latent image effects result in dark streaks to the north-west and southeast of the galaxy centre at the edge of the region detected at  $70\ \mu\text{m}$  (at  $\alpha = 7:37:20\ \delta = +65:40:00$  and  $\alpha = 7:36:35\ \delta = +65:32:00$ ). Our algorithms tend to exclude the emission from these regions, so the latent image effects only have a very minor impact on the analysis.

We performed several analysis steps in using  $70$  and  $160\ \mu\text{m}$  flux densities to calculate dust masses. First, we convolved the  $70\ \mu\text{m}$  data with a kernel that matches the PSF of the data to the PSF of the  $160\ \mu\text{m}$  data (see Sec. 2.5 below). Next, we regridded the  $160\ \mu\text{m}$  data so that its coordinate system matched the  $70\ \mu\text{m}$  data. After this step, we only used data for pixels detected at the  $10\sigma$  level in the convolved data for each wave band so that systematic effects such as offsets in the background would not strongly affect the results. We proceeded to fit blackbodies  $B_\nu(T)$  with temperatures  $T$  modified by  $\lambda^{-2}$  emissivity functions to the  $70$  and  $160\ \mu\text{m}$  data for each pixel meeting this signal-to-noise criterion so as to determine the approximate dust temperatures. Following this, we calculated dust masses within individual pixels using

$$M_{\text{dust}} = \frac{D^2 f_\nu}{\kappa_\nu B_\nu(T)}, \quad (3)$$

which is a variant of an equation derived by Hildebrand (1983). In this equation,  $D$  is the distance to the galaxy,  $f_\nu$  is the flux density,  $\kappa_\nu$  represents the absorption opacity of the dust, and  $B_\nu(T)$  is the blackbody function for the best fitting temperature  $T$ . We used the  $160\ \mu\text{m}$  flux densities in Equation 3 because the data were taken from the Rayleigh-Jeans side of the thermal dust emission and are therefore less sensitive to uncertainties in temperature. The value for  $\kappa_\nu$  at  $160\ \mu\text{m}$  is given by Li & Draine (2001) as  $12.0\ \text{cm}^2\ \text{g}^{-1}$ . The dust masses were then converted to dust surface densities by dividing the pixels by their surface area in  $\text{pc}^2$ . As a test of the robustness of the results against systematic offsets in the background, we increased the background in one wave band by  $3\sigma$ , decreased it in the other by  $3\sigma$ , and then measured the total dust mass and the exponential scale length of the radial profile for the dust surface density (described in Section 5). We found that the dust mass only varied  $< 10\%$  and that the scale length varied by only  $1\sigma$  when this was done, even though systematic offsets of this magnitude seem highly unrealistic.

This is a simplistic approach to calculating dust masses, but it should provide approximate measurements of the dust masses within this galaxy. More sophisticated dust models, such as those presented by Dale & Helou (2002) and Draine et al. (2007), include multiple thermal components of dust heated by radiation fields with variable strengths and also account for the different spectral energy distributions of grains of different sizes. Unfortunately, those models include many free parameters, and so when only two wave bands are available for defining the far-infrared dust SED, as is the case for our analysis of subregions in NGC 2403, we cannot accurately apply complex dust SED models. Fortunately, when the dust masses predicted by the models of Draine et al. (2007) are compared with the dust masses calculated using a single thermal component fit to  $\geq 70\ \mu\text{m}$  data, the masses agree to within a factor of 2-4 (Regan et al. 2004; Bendo et al. 2006). Therefore, the dust masses estimated from a single thermal component should still be useful for our analysis.

It is possible that the observations here may have missed the presence of very cold dust (dust with temperatures  $< 15\ \text{K}$ ) that may not contribute strongly to the  $70$  and  $160\ \mu\text{m}$  bands but that may constitute the bulk of the dust mass within this galaxy. If present, this very cold dust emission would be detected at 200-

1000  $\mu\text{m}$ . Unfortunately, we do not have any useful data with which to search for the presence of such emission. Some archival JCMT SCUBA data are available, but nothing is detected with a signal-to-noise level of  $> 3$  in the data. Moreover, it is unclear whether submillimetre emission that exceeds thermal dust emission models fit to  $< 200 \mu\text{m}$  originates from large masses of cold dust or from dust with unexpectedly high submillimetre emissivities. In any case, most current studies on this subject suggest that the 70 and 160  $\mu\text{m}$  bands can be used without submillimetre data to produce reasonably accurate estimates of the dust mass. See Appendix A for an extended discussion.

## 2.3 CO data

### 2.3.1 CO $J=(3-2)$ data

The CO  $J=3-2$  line observations were obtained at the JCMT as part of the JCMT NGLS, using the 16 element heterodyne array HARP-B with the backend spectrometer ACSIS (Buckle et al. 2009). The FWHM of the beam is 14.5 arcsec. We give an overview of the observation and data reduction procedures here. For a more detailed explanation of the general JCMT NGLS observing and data reduction process for raster maps see Warren et al. (2009, submitted).

Observations for NGC 2403 by the JCMT NGLS took place over two runs in November 2007 and January 2008. We mapped the galaxy using a basketweave raster scanning method, with half array steps between scan rows/columns. The target area was a rectangular region with a position angle of  $127^\circ$  rotated from north through east and with a size of  $11.7 \text{ arcmin} \times 6.2 \text{ arcmin}$ , which corresponds to half of the optical diameter along both the major and minor axes. The correlator was configured to have a bandwidth of  $\sim 1 \text{ GHz}$  and a resolution of 0.488 MHz ( $0.43 \text{ km s}^{-1}$  at the frequency of the  $^{12}\text{CO } J=3-2$  transition) centered at  $121 \text{ km s}^{-1}$ . For each scan, we integrated for 5 s per pointing within the target field, and scans were repeated until we reached the target RMS for the survey (19 mK ( $T_{\text{A}}^*$ ) after binning to  $20 \text{ km s}^{-1}$  resolution). After rejecting one half of an individual scan that failed the survey quality assurance criteria, the total integration time was up to 62.5 seconds per point (depending on the number of contributing receptors that were not flagged or missing in the array).

Data reduction and most of the analysis were carried out with the version of the Starlink software package that is maintained by the Joint Astronomy Centre (Currie et al. 2008)<sup>3</sup>. First, data for individual receptors with bad baselines were flagged and removed from the data. Generally, two to four receptors in a scan were flagged. After this, the raw scans were combined into a data cube using a  $\text{sinc}(\pi x)\text{sinc}(k\pi x)$  kernel as the weighting function to determine the contribution of individual receptors to each pixel. The  $\text{sinc}(\pi x)\text{sinc}(k\pi x)$  function was used instead of other weighting functions because it significantly reduces the noise in the maps while having a very minor effect on the resolution. The resulting cube was then trimmed to remove the leading and trailing scan ends outside the target field, where the scan coverage is incomplete. A mask was created to identify line-free regions of the data cube, and a third-order baseline was fit to those line-free regions. The clumpfind algorithm (Williams et al. 1994), implemented as part of the Starlink/CUPID task findclumps (Berry et al. 2007), was used to identify regions with emission above two times the rms noise in a data cube that had been boxcar smoothed by 3 pixels and 25

velocity channels. Moment maps were created from the original data cube using a mask created from findclumps. We converted the CO  $J=(3-2)$  data from corrected antenna temperature ( $T_{\text{A}}^*$ ) to the main beam temperature scale by dividing by  $\eta_{\text{MB}} = 0.60$ . The CO  $J=(3-2)$  emission is not detected beyond radii of  $\sim 3.75 \text{ kpc}$  (which corresponds to an angular scale of  $\sim 250 \text{ arcsec}$  along the major axis).

For some of the analysis in this paper, the CO  $J=(3-2)$  emission is converted into molecular gas surface density. The conversion factor is dependent on a comparison between the CO  $J=(3-2)$  and  $J=(1-0)$  line emission. We discuss both of these topics in Section 4.

### 2.3.2 CO $J=(1-0)$ data

We compared the CO  $J=(3-2)$  data with CO  $J=(1-0)$  data from two sources. We primarily used CO  $J=(1-0)$  data taken by Thornley & Wilson (1995) using the National Radio Astronomy Observatory (NRAO) 12 meter telescope. The observations were performed as a series of pointings separated by 30 arcsec that approximately cover the central  $5.5 \text{ arcmin} \times 4 \text{ arcmin}$  of the galaxy. These data have a FWHM of 54 arcsec and a spectral resolution of  $2.6 \text{ km s}^{-1}$ . Since the spacing between the pointings is smaller than the beam, we can treat these data as a fully sampled map. Table 1 by Thornley & Wilson (1995) gives the integrated line intensities (based on main beam temperatures) and uncertainties that they measured in individual pointings across the optical disc of the galaxy; we used these data to construct a CO  $J=(1-0)$  image. Upper limits were treated as 0 for our analysis. See Thornley & Wilson (1995) for additional details on the observations and data reduction.

We also had access to CO  $J=(1-0)$  data taken in the BIMA Survey of Nearby Galaxies (SONG; Helfer et al. 2003). While the  $6.3 \times 5.8 \text{ arcsec}$  FWHM of the beam for the data is superior to that for both HARP-B and the NRAO 12 m data, the BIMA SONG data have problems that make it less suitable for our analysis. A comparison of the BIMA SONG data to the NRAO 12 m data revealed that only  $\sim 60\%$  of the flux was recovered (Helfer et al. 2003), and the area in which sources are detected in the BIMA SONG data is significantly smaller than that for either the HARP-B or NRAO 12 m data. While we still use the BIMA SONG data for a qualitative comparison to other data, we will not use it for quantitative comparisons.

## 2.4 HI data

The HI data used for this analysis were taken by THINGS (Walter et al. 2008). The observations were performed with the Very Large Array in the B, C, and D configurations, which ensured fairly uniform sensitivity from the largest scales all the way to the resolution limit set by the long baselines of B-array. Calibrated, continuum-subtracted data cubes were created using the Astronomical Image Processing System. The uncertainties are dominated by the calibration uncertainty, which is 5%.

THINGS released two data products that differ based on the weighting of the data. We used the data with the natural weighting. In these data, all visibility points in the  $uv$  plane are weighted equally. Large-scale structures, including the diffuse, extended HI emission that may be associated with diffuse interstellar dust, should be more easily detected in the data with the natural weighting. The FWHM of the PSF for the naturally weighted data is  $8.75 \times 6.75 \text{ arcsec}$ . According to Walter et al. (2008), a comparison between the VLA data and single-dish data from the literature compiled by Paturel et al. (2003) showed a strong agreement for most

<sup>3</sup> Available for download from <http://www.jach.hawaii.edu>.

**Table 1.** PSFs Used for Creating Convolution Kernels

Telescope / Instrument	Wavelength	FWHM (arcsec)	Source
<i>Spitzer</i> / IRAC	3.6 $\mu\text{m}$	1.7	Model (STinyTim)
	8.0 $\mu\text{m}$	2.0	Model (STinyTim)
<i>Spitzer</i> / MIPS	70 $\mu\text{m}$	18	Empirical
	160 $\mu\text{m}$	38	Empirical
JCMT / HARP-B	CO $J=(3-2)$	14.5	Gaussian function
NRAO 12 m	CO $J=(1-0)$	54	Gaussian function
VLA	HI	$8.75 \times 6.75$	Gaussian function <sup>a</sup>

<sup>a</sup> The position angle of the major axis is  $25.2^\circ$  from north to east.

THINGS galaxies including NGC 2403, indicating that significant emission is not missing from the VLA data because of gaps in the coverage of the  $uv$  plane. See Walter et al. (2008) for additional details on the observations and data reduction as well as the reliability of the data. To convert the surface brightnesses  $S_\nu$  to atomic gas surface densities  $\sigma_{dust}$  on a pixel-by-pixel basis, we used the equation

$$\frac{\sigma_{dust}}{\text{M}_\odot \text{pc}^{-2}} = 8870 \left( \frac{S_\nu}{\text{Jy beam}^{-1} \text{km s}^{-1}} \right) \left( \frac{\text{arcsec}^2}{\text{FWHM}_{maj} \text{FWHM}_{min}} \right) \quad (4)$$

based on equations given by Walter et al. (2008).

## 2.5 Convolution kernels

The various images described above have PSFs with varying widths, and the shapes of the PSFs vary as well. In particular, the *Spitzer* PSFs have very pronounced Airy rings whereas most other PSFs can be approximated as Gaussian functions. To properly compare the data to each other, we need convolution kernels that not only match the FWHMs of the PSFs to each other but also match the shapes to each other.

We created kernels for this purpose following the instructions given by Gordon et al. (2008). We first generated images that represented the PSFs in the individual wave bands. For the CO  $J=(3-2)$ , CO  $J=(1-0)$ , and HI data, we used Gaussian functions. For the 3.6 and 8  $\mu\text{m}$  data, we used PSFs produced with STinyTim<sup>4</sup>, a PSF simulator designed for *Spitzer* (Krist 2002). For the 70 and 160  $\mu\text{m}$  data, we used empirically-determined PSFs created from extragalactic observations of point-like extragalactic sources (see Young et al. 2009, for additional information). Table 1 gives a summary of these PSFs.

We then used the equation

$$K(x, y) = F^{-1} \left[ \frac{W(\omega) F[PSF_2(x, y)]}{F[PSF_1(x, y)]} \right] \quad (5)$$

to create convolution kernels  $K(x, y)$  that match  $PSF_1$  to  $PSF_2$ .  $F$  is a Fourier transform,  $W(\omega)$  is a radial Hanning truncation function given by

$$W(\omega) = \begin{cases} \frac{1}{2} \left[ 1 + \cos \left( \frac{2\pi\omega}{\omega_0} \right) \right] & \omega \leq \omega_0 \\ 0 & \omega > \omega_0 \end{cases} \quad (6)$$

that is used to suppress high-frequency spatial noise in the resulting kernels. For each kernel, we adjusted  $\omega_0$  to produce kernels which,

when visually inspected, contained as much structure related to the PSF transformation as possible while excluding high frequency noise. However, for converting from one idealized Gaussian profile to another, we created convolution kernels using the equation

$$K(r) = e^{-r^2/2(\sigma_2^2 - \sigma_1^2)} \quad (7)$$

where  $\sigma_1$  is the width of the narrower Gaussian function that is being blurred to match the width  $\sigma_2$  of the broader Gaussian function.

The final kernels that we created convert data to match two different PSFs. For comparing PAH emission to atomic or molecular gas, the kernels match the data to the PSFs of the CO  $J=(3-2)$  data. For comparing gas and dust emission, the kernels match the data to the PSFs of the 160  $\mu\text{m}$  data. For the comparison between the CO  $J=(3-2)$  and  $J=(1-0)$  data, the PSFs of the data were matched to the PSF of the NRAO data. Note that we used a pre-made kernel created by K. D. Gordon for matching the PSF of the 70  $\mu\text{m}$  data to that of the 160  $\mu\text{m}$  data<sup>5</sup>. The convolution kernels were applied to the CO  $J=(3-2)$  data before spectral line extraction.

## 2.6 Abundance information

Since metallicity has been shown to have a possible effect on the CO to  $\text{H}_2$  conversion factor (discussed further in Section 4) and since metallicity variations could explain variations in gas-to-dust ratios (discussed further in Section 5), we need abundance gradient information for our analyses. Many authors have measured and published gradients in  $12+\log(\text{O}/\text{H})$  within this galaxy, including Fierro et al. (1986), Vila-Costas & Edmunds (1992), Zaritsky et al. (1994), Garnett et al. (1997) and van Zee et al. (1998). After scaling the various gradients so that they correspond to a galaxy distance of 3.13 Mpc, we find that the  $12+\log(\text{O}/\text{H})$  gradients vary from  $-0.0774 \pm 0.0014$  dex  $\text{kpc}^{-1}$  (van Zee et al. 1998) to  $-0.098 \pm 0.009$  dex  $\text{kpc}^{-1}$  (Garnett et al. 1997) with a mean of  $-0.084$  dex  $\text{kpc}^{-1}$  and a standard deviation of  $0.009$  dex  $\text{kpc}^{-1}$ . The value of  $12+\log(\text{O}/\text{H})$  at the centre of the galaxy is also given by Vila-Costas & Edmunds (1992), Zaritsky et al. (1994), and van Zee et al. (1998); the mean of their measurements is 8.4 with a standard deviation of 0.13. We use these values for the abundance gradients in NGC 2403. Compared to the abundance gradients for other galaxies reported by Vila-Costas & Edmunds (1992) and Zaritsky et al. (1994), both of whom worked with relatively large samples, the abundance gradients measured in NGC 2403 are rather typical.

Although the studies cited above report consistent  $12+\log(\text{O}/\text{H})$  gradients for NGC 2403, more recent observations of abundance gradients in other galaxies have shown that the methods used in the above references may contain systematic errors (Pilyugin 2001; Bresolin et al. 2004; Rosolowsky & Simon 2008, e.g.). Moreover, newer methods for calculating oxygen abundances show that the gradients may be significantly shallower. However, because no abundance gradient data for NGC 2403 has been published using these newer techniques, we will use these older abundance gradients for now but discuss how shallower abundance gradients could affect the results where appropriate.

<sup>4</sup> Available from <http://ssc.spitzer.caltech.edu/archanaly/contributed/browse.html>.

<sup>5</sup> The kernel is available at [http://dirty.as.arizona.edu/~kgordon/mips/conv\\_psf/conv\\_psf.html](http://dirty.as.arizona.edu/~kgordon/mips/conv_psf/conv_psf.html).

## 3 IMAGES

Figure 1 shows in their native resolution the  $3.6\ \mu\text{m}$ ,  $8.0\ \mu\text{m}$ ,  $70\ \mu\text{m}$ ,  $160\ \mu\text{m}$ , CO  $J=(3-2)$ , and HI images for the entire optical disc of the galaxy. In addition, Figure 2 shows the inner  $12 \times 9$  arcmin for all of these images as well as the CO  $J=(1-0)$  images from the NRAO 12 m telescope and from the BIMA SONG survey. In interpreting these images, we will refer to the HII region marked with the cyan square in Figure 2 as VS 44. This is region 44 in the catalogue produced by (Véron & Sauvayre 1965), and it corresponds to region 128 in the atlas of HII regions mapped by Hodge & Kennicutt (1983). VS 44 is the brightest source of both H $\alpha$  emission (Drissen et al. 1999) and  $24\ \mu\text{m}$  emission (Bendo et al. 2008) and therefore is the site with the strongest star formation activity in the galaxy. Since the region is located well outside the nucleus, it can be used to distinguish between effects related to radius and effects related to star formation activity or infrared surface brightness.

The stellar emission, which is shown by the  $3.6\ \mu\text{m}$  image, looks similar to what is expected for a late-type spiral galaxy; the bulge is close to non-existent, and the disc, while well-defined, has a clumpy structure. The PAH  $8\ \mu\text{m}$  image shows the clumpy dust structures in the ISM. Some of this structure is also visible in the  $70$  and  $160\ \mu\text{m}$  images despite the lower resolution of the data. The dust structure is fairly typical compared to most late-type spiral galaxies (Bendo et al. 2007). The CO  $J=(3-2)$  and  $J=(1-0)$  images all appear similar to each other. Some of the structures seen in the CO emission, such as the spiral arm structure to the west of the centre and a few CO-bright regions like VS 44, are similar to those traced by PAH and longer-wavelength dust emission. However, the CO maps contain a notable hole close to the centre of the optical disc, whereas PAH  $8\ \mu\text{m}$  and longer-wavelength dust emission is still present in this region. Interestingly, this hole corresponds to the peak in diffuse X-ray emission found by Fraternali et al. (2002). We discuss this further in Sections 5 and 6. In contrast to all of these images, the HI emission is much more extended; the emission is detectable well outside the optical disc of the galaxy. A number of shell-like structures are visible within the HI data. These shells were also identified by Thilker et al. (1998), who associated them with star-forming regions. While bright objects in many of the other wave bands, such as VS 44, do not have HI counterparts, some of the shells in the HI image, such as the ones at  $\alpha = 7:37:15$   $\delta = +65:34:30$  and  $\alpha = 7:36:50$   $\delta = +65:37:30$ , do have counterparts in other wave bands.

Figure 3 and 4 show the dust surface density and temperature maps derived as part of the analysis in Section 2.2. The dust mass image exhibits structures that appear similar to those seen at  $70$  and  $160\ \mu\text{m}$ . However, star-forming regions appear notably enhanced in the temperature map. The dust temperatures range from  $26\ \text{K}$  in infrared-bright regions (including VS 44) to  $17\ \text{K}$  in the fainter diffuse regions. Note that the  $< 20\ \text{K}$  regions located at approximately  $\alpha = 7:37:20$   $\delta = +65:40:00$  and  $\alpha = 7:36:35$   $\delta = +65:32:00$  may have been affected by latent image effects in the  $70\ \mu\text{m}$  band. The median temperature is  $22\ \text{K}$ . These temperatures are similar to those measured in other nearby galaxies when single thermal components have been fit to far-infrared ISO or *Spitzer* data that sample the peak of the thermal dust emission from  $60$  to  $200\ \mu\text{m}$  (e.g. Popescu et al. 2002; Bendo et al. 2003; Engelbracht et al. 2004; Regan et al. 2004; Bendo et al. 2006; Perez-Gonzalez et al. 2006).

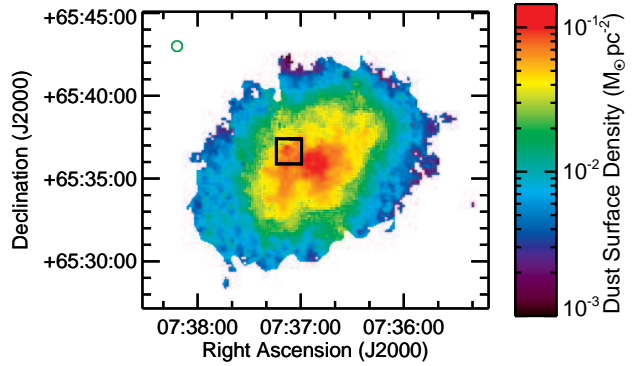


**Figure 3.** Image of the dust surface density in NGC 2403 produced after the analysis in Section 2.2. The surface densities were corrected for the inclination of this galaxy (given as  $62.9^\circ$  by de Blok et al. (2008)). The image size and orientation is the same as the size and orientation of the images in Figure 1. The green circle in the upper left corner shows the  $38$  arcsec FWHM of the PSF, which is equivalent to the PSF of the  $160\ \mu\text{m}$  data. The uncertainties in the data are  $\sim 20\%$ . The black square indicates the location of VS 44.

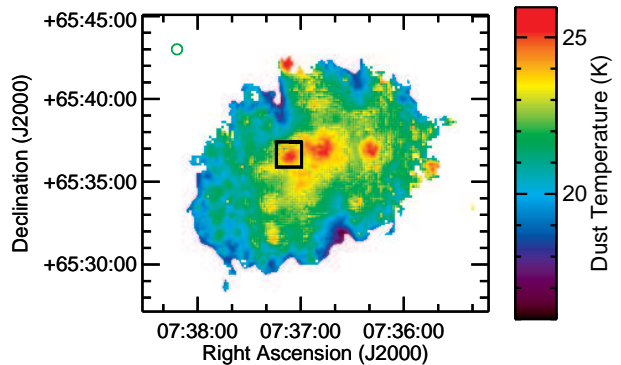


**Figure 4.** Image of the dust temperatures in NGC 2403 produced after the analysis in Section 2.2. The image size and orientation is the same as the size and orientation of the images in Figure 1. The green circle in the upper left corner shows the  $38$  arcsec FWHM of the PSF, which is equivalent to the PSF of the  $160\ \mu\text{m}$  data. The uncertainties are  $\lesssim 1\ \text{K}$ . The black square indicates the location of VS 44. Regions with temperatures of  $< 20\ \text{K}$  at  $\alpha = 7:37:20$   $\delta = +65:40:00$  and  $\alpha = 7:36:35$   $\delta = +65:32:00$  may have been strongly affected by latent image effects.

#### 4 THE CO $J=(3-2)/J=(1-0)$ RATIO AND THE CONVERSION FROM LINE INTENSITY TO MOLECULAR GAS SURFACE DENSITY

Given the superior resolution of the HARP-B CO  $J=(3-2)$  data compared to the older NRAO 12 m CO  $J=(1-0)$  data and given the superior spatial coverage of the HARP-B data to both the NRAO 12 m and BIMA SONG data, it would be preferable to use the HARP-B data to calculate molecular gas surface densities for comparisons to dust emission, particularly PAH  $8\ \mu\text{m}$  emission. However, the conversion from CO line emission to molecular gas mass ( $X_{\text{CO}}$ ) is generally based on the CO  $J=(1-0)$  line. Therefore, the CO  $J=(3-2)/J=(1-0)$  ratio needs to be determined to convert the CO  $J=(3-2)$  line to a molecular gas surface density.



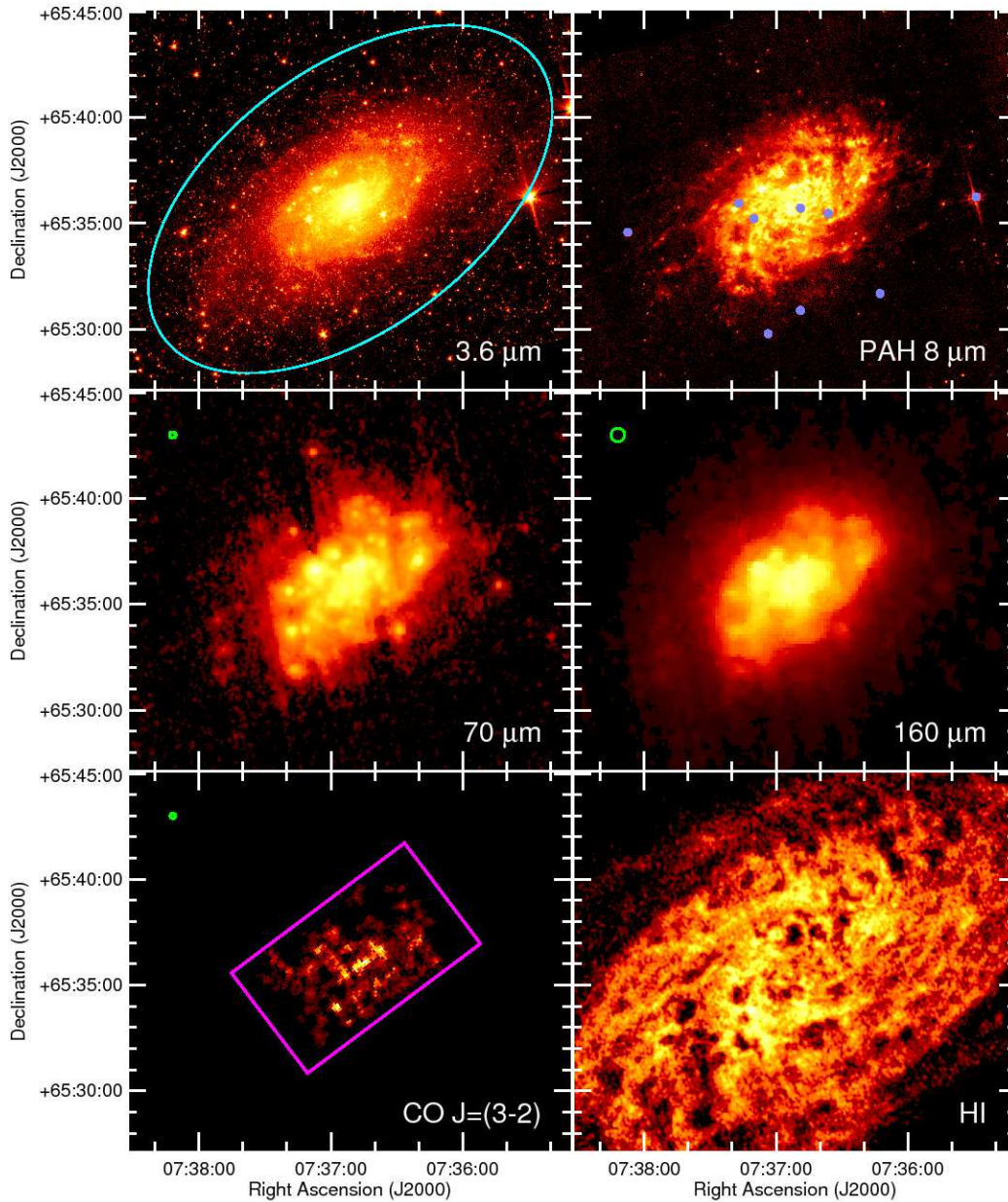


**Figure 1.** Images of the entire optical disc of NGC 2403 in multiple wave bands. The  $3.6 \mu\text{m}$  image traces starlight. The PAH  $8 \mu\text{m}$  image traces primarily PAH emission. The  $70$  and  $160 \mu\text{m}$  images trace cold dust emission. The CO  $J=(3-2)$  image shows CO emission associated with molecular gas. The HI image shows atomic gas emission. All images are  $21 \text{ arcmin} \times 18 \text{ arcmin}$  with north up and east to the left. Logarithmic colour scales are used for all images except the  $160 \mu\text{m}$  image, where the logarithmic scale to the second power was used to enhance the structure in the image, and the CO  $J=(3-2)$  image, where a linear colour scale was used. The colour scales were selected so as to best enhance the structures visible in the optical disc of the galaxy. Green circles in the upper left corners of the images show the beam size when the FWHM is greater than 10 arcsec; smaller beam sizes are difficult to illustrate in this image. The optical disc of the galaxy as defined by de Vaucouleurs et al. (1991), is shown as a cyan ellipse in the  $3.6 \mu\text{m}$  image. The blue circles in the PAH  $8 \mu\text{m}$  image show the positions of foreground stars that were brighter than or as bright as the continuum emission from the galaxy at  $8 \mu\text{m}$ . These stars were masked out in the analysis. The magenta box in the CO  $J=(3-2)$  image shows the region observed with HARP-B. Pixels with non-detections in the CO data are set to black.

For this analysis, we compared the HARP-B CO  $J=(3-2)$  data to the NRAO 12 m CO  $J=(1-0)$  data from Thornley & Wilson (1995) for the reasons discussed in Section 2.3.2. We examined both median line intensities and intensities measured in the pointing positions used by Thornley & Wilson (1995). For these compar-

isons, we use intensities based on the main beam temperatures. For comparing median line intensities, we used CO  $J=(3-2)$  data where the resolution and pixels are matched to those of the CO  $J=(1-0)$  data, and we only selected pixels that are  $3\sigma$  detections in both images. The median CO  $J=(1-0)$  line intensity in these pixels is

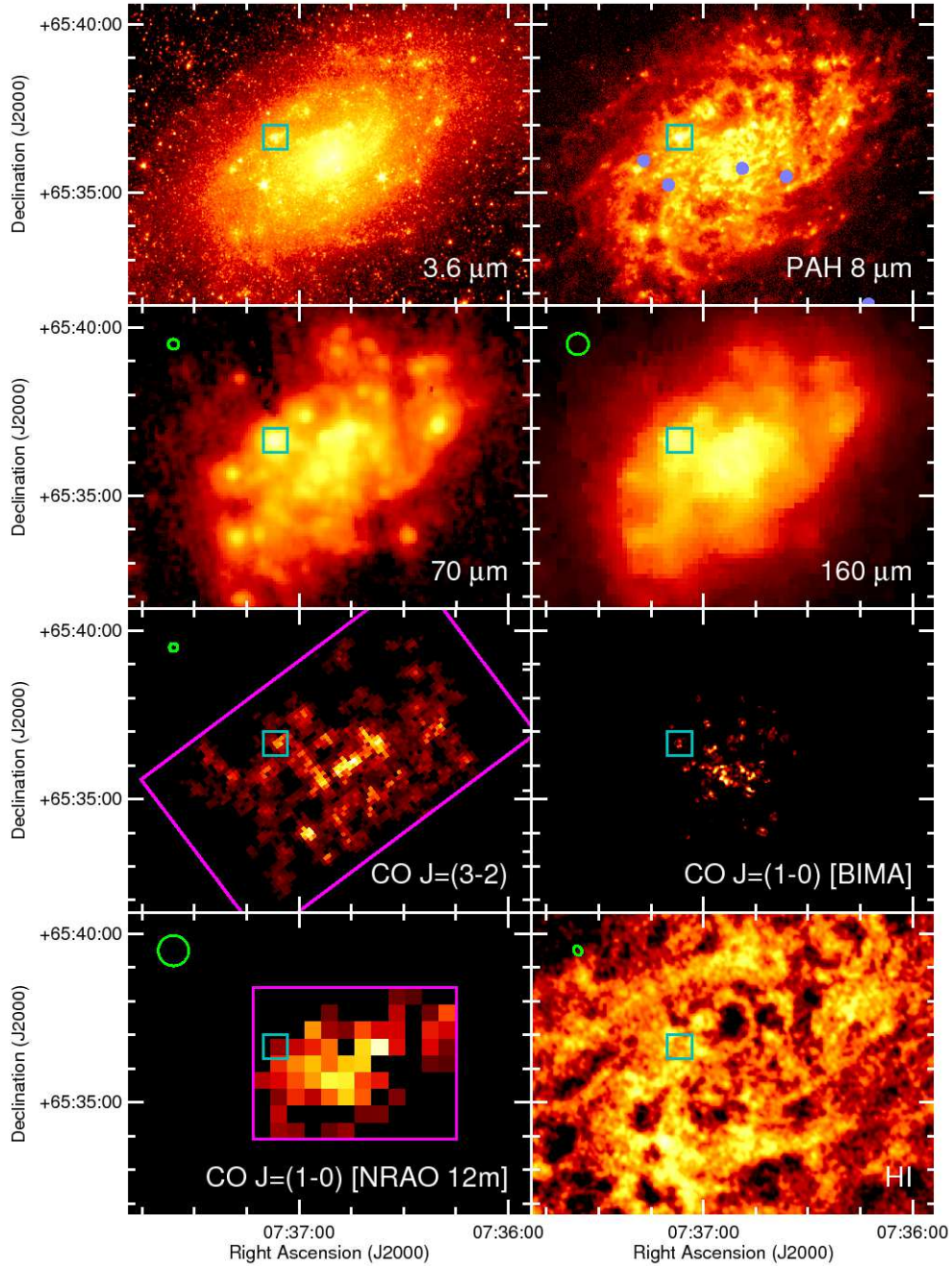


**Figure 2.** Images of the inner  $12 \times 9$  arcmin of NGC 2403 in multiple wave bands. The  $3.6 \mu\text{m}$ ,  $8.0 \mu\text{m}$ ,  $70 \mu\text{m}$ ,  $160 \mu\text{m}$ , CO  $J=(3-2)$ , and HI images are the same as the images in Figure 1 except that the images are cropped and that the colour scales have been adjusted to show greater contrast in the centre. The colours in the two additional CO  $J=(1-0)$  images (from the BIMA SONG survey and from the NRAO 12 m observations by Thornley & Wilson (1995)) are scaled linearly. The magenta box in the CO  $J=(1-0)$  image from the NRAO 12 m shows the region that was covered in the observations. Pixels with non-detections in the CO data are set to black. The cyan square indicates the location of VS 44, which is region 44 in the catalogue by (Véron & Sauvayre 1965) and region 128 in the catalogue by Hodge & Kennicutt (1983). See the caption for Figure 1 for additional information on the other symbols and lines in the figure.



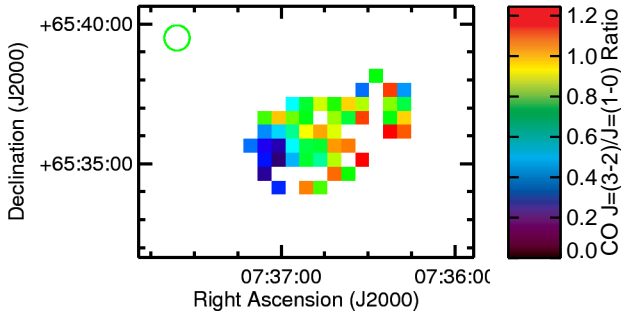


**Figure 5.** Image of the ratio of the CO  $J=(3-2)/J=(1-0)$  line ratio for the central  $12 \times 9$  arcmin of NGC 2403. The orientation, size, and central coordinates of the image have been selected to match those of Figure 2. The 30 arcsec pixels correspond to the positions of the pointed observations performed by Thornley & Wilson (1995). To make this plot, the PSF of the data in the CO  $J=(3-2)$  data cube were matched to the PSF of the CO  $J=(1-0)$  data, the CO  $J=(3-2)$  line intensities were measured, and then the CO  $J=(3-2)$  data were rebinned to match the pixel scale of the CO  $J=(1-0)$  data. The green circle in the upper left corner shows the 54 arcsec PSF of the CO  $J=(1-0)$  data. The uncertainties in this ratio are mainly dependent on the uncertainties in the CO  $J=(1-0)$  data; the typical signal-to-noise values of the ratios range from  $3\sigma$  to  $8\sigma$ . Locations where line emission was not measured above the  $3\sigma$  level and locations affected by artifacts along the edge of the region observed in the CO  $J=(3-2)$  line were left blank.

$1.56 \text{ K km s}^{-1}$ , while the median CO  $J=(3-2)$  intensity is  $1.08 \text{ K km s}^{-1}$ . This gives a median CO  $J=(3-2)/J=(1-0)$  line ratio of 0.69. The standard deviation of the ratio across the disc is 0.29. Figure 5 shows how the line ratio varies across the centre of the galaxy. The ratio does not appear to exhibit any clear structure, although the ratio is low in the southeast side of the region, which corresponds to a location where the CO  $J=(3-2)$  ratio is also low. The ratios range from  $0.11 \pm 0.3$  to  $1.2 \pm 0.3$ .

For comparison, Thornley & Wilson (1994) and Wilson et al. (1997) measured ratios for individual giant molecular clouds in M33 ranging from 0.4 to 0.8, and Mauersberger et al. (1999) measured CO  $J=(3-2)/J=(1-0)$  ratios in 28 nearby spiral galaxies ranging from 0.2 to 0.7. The median CO  $J=(3-2)/J=(1-0)$  ratio for NGC 2403 appears high but typical compared to these other measurements. However, the factor of 10 variation in the CO  $J=(3-2)/J=(1-0)$  ratio across the disc of NGC 2403 is high compared to what was measured by these other surveys, and the minimum and maximum fall outside the typical ranges of the objects in the other surveys. It is quite possible that the variations in the ratio that we observed in NGC 2403 are real and that such variations have not been observed in other surveys either because the the regions were unresolved or undetected. Wilson et al. (2009) using CO  $J=(3-2)$  data from the JCMT NGLS found evidence for CO  $J=(3-2)/J=(1-0)$  ratios that vary by a factor of 10 in NGC 4569 as well. It could be possible that further analysis of the JCMT NGLS data will reveal that such variations are actually typical for nearby galaxies.

Given the strong variations in the ratio, we did not feel confident about applying a simple scaling term to the CO  $J=(3-2)$  data to scale it to match the CO  $J=(1-0)$  data. We therefore examined how the CO  $J=(3-2)/J=(1-0)$  ratio could be derived from either the radius or the CO  $J=(3-2)$  surface brightness. For this analysis, we used the CO  $J=(3-2)$  and  $J=(1-0)$  data that were prepared for Figure 5. A fit between  $\log(\text{CO } J=(3-2)/J=(1-0))$  and a linear function of both  $\log(\text{CO } J=(3-2)/(\text{K km s}^{-1}))$  and radius (calculated using

the inclination of  $62.9^\circ$  given by de Blok et al. (2008)) resulted in the lowest reduced  $\chi^2$  value. The relation is

$$\log\left(\frac{I_{\text{CO } J=(3-2)}}{I_{\text{CO } J=(1-0)}}\right) = (0.70 \pm 0.07) \log\left(\frac{I_{\text{CO } J=(3-2)}}{\text{K km s}^{-1}}\right) + (0.088 \pm 0.014) \left(\frac{r}{\text{kpc}}\right) - (0.38 \pm 0.03). \quad (8)$$

Figure 6 shows the relation between the CO  $J=(3-2)/J=(1-0)$  intensity ratio and CO  $J=(3-2)$  intensity, the relation between the intensity ratio and radius, and the relation given by Equation 8. The dependence of the ratio on CO  $J=(3-2)$  intensity is very apparent, but the dependence of the ratio on radius is fairly weak. Nonetheless, including a term for radius in the conversion between the CO  $J=(3-2)$  intensity and the CO  $J=(3-2)/J=(1-0)$  ratio does provide a better fit (in terms of the reduced  $\chi^2$ ) than a function that does not include such a term. We also found that the Pearson's correlation coefficient increased from 0.54 for the data in the left panel of Figure 6 to 0.81 for the data in the right panel, confirming that the extra radial distance term reduced the scatter. Based on the scatter around the relation given in Equation 8, the conversion from the CO  $J=(3-2)$  intensity to the CO  $J=(1-0)$  intensity should be accurate to within 20%.

Given these results, we can now scale the CO  $J=(1-0)$  to  $\text{H}_2$  conversion factor for use with the CO  $J=(3-2)$  line.  $X_{\text{CO}}$  for the  $J=(1-0)$  transition may depend on several environmental factors. In particular, it has been shown that it may be dependent on metallicity (e.g. Wilson 1995; Israel 1997, 2000; Barone et al. 2000; Israel et al. 2003; Strong et al. 2004; Israel 2005). We have decided to use the conversion

$$\log(X_{\text{CO } J=(1-0)}) = 12.2 - 2.5 \log[\text{O}/\text{H}] \quad (9)$$

proposed by Israel (2000), which is based on determining the  $X_{\text{CO } J=(1-0)}$  needed to keep the ratio of total gas surface density to far-infrared surface brightness constant in CO clouds in the Large and Small Magellanic Clouds. This equation is also found to be in agreement with measurements based on gamma-ray emission from the Milky Way (Strong et al. 2004). We use this equation along with the abundance gradients given in Section 2.6 in one set of calculations of the molecular gas surface densities.

However, recent observational results in which the CO velocity dispersions, radii, and CO luminosities of giant molecular clouds are used to infer their mass and hence  $X_{\text{CO } J=(1-0)}$  suggest that the conversion factor does not vary with metallicity (Blitz et al. 2007; Bolatto et al. 2008), contradicting the results derived using other methods. Therefore, we also use a second set of molecular gas surface density data calculated using  $X_{\text{CO } J=(1-0)} = 1.9 \times 10^{20} \text{ cm}^{-2} (\text{K km s}^{-1})^{-1}$ , which was derived by Strong & Mattox (1996) using models of gamma ray scattering that did not include radial variations.

Israel (1997) indicated that radiation field strength could be a second factor that affects  $X_{\text{CO}}$ , although some authors have not found evidence for such a dependency (e.g. Bolatto et al. 2008). The application of the relation found by Israel (1997) to our data does not appear straightforward. The metric for radiation field intensity used by Israel (1997) uses the ratio of the far-infrared surface brightnesses measured using IRAS data to the neutral hydrogen density. Because IRAS data does not sample the Rayleigh-Jeans side of the dust SED in the same way that *Spitzer* data does, we would need to convert the far-infrared fluxes derived from *Spitzer* data to match that calculated from IRAS data, which may not be straightforward. Moreover, Israel (1997) derived his relation using subregions within dwarf galaxies where radial variations in abundances were not present and therefore where variations in the

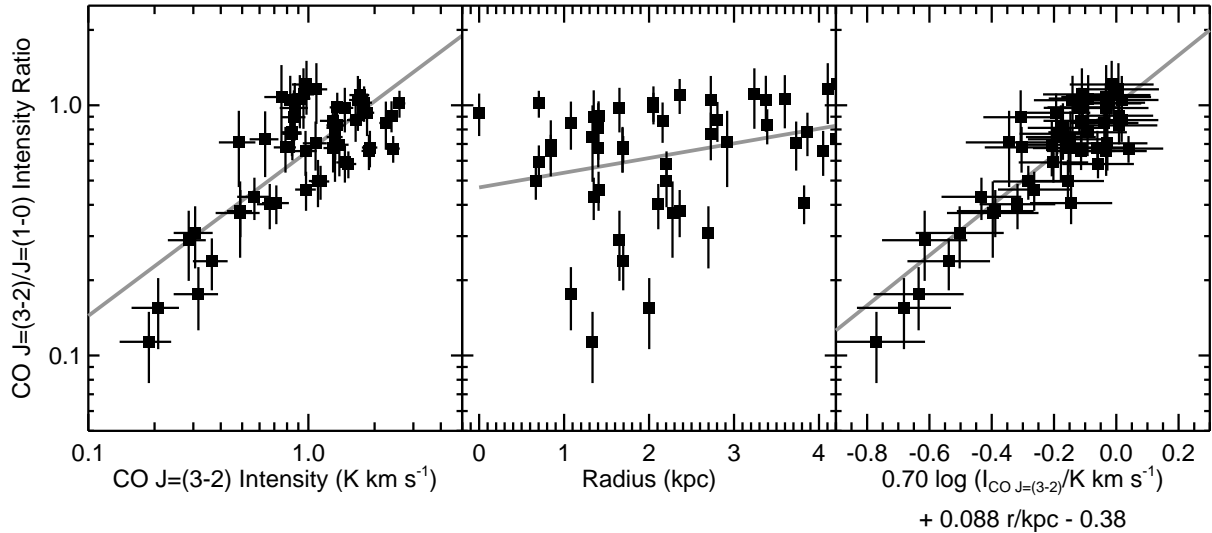


**Figure 6.** The CO  $J=(3-2)/J=(1-0)$  intensity ratio plotted as a function of CO  $J=(3-2)$  intensity (left panel), radius (center panel), and the right hand side of Equation 8 (right panel). The data points are for the 30 arcsec square regions shown in Figure 5. The grey lines are the best fit lines to the data.

gas-to-dust ratio should not be present, whereas NGC 2403 clearly exhibits radial variations in abundances and therefore may exhibit radial variations in the gas-to-dust ratio that would affect the radiation field intensity metric. Fortunately, Israel (1997) found that it should still be possible to derive a reasonable approximation for  $X_{CO}$  based on its relation to oxygen abundances alone. Therefore, for simplicity, we will not attempt to include an additional correction to  $X_{CO}$  for radiation field intensity, although we still discuss the implications of this dependency when appropriate.

## 5 COMPARISON OF ATOMIC GAS, MOLECULAR GAS, AND DUST SURFACE DENSITIES

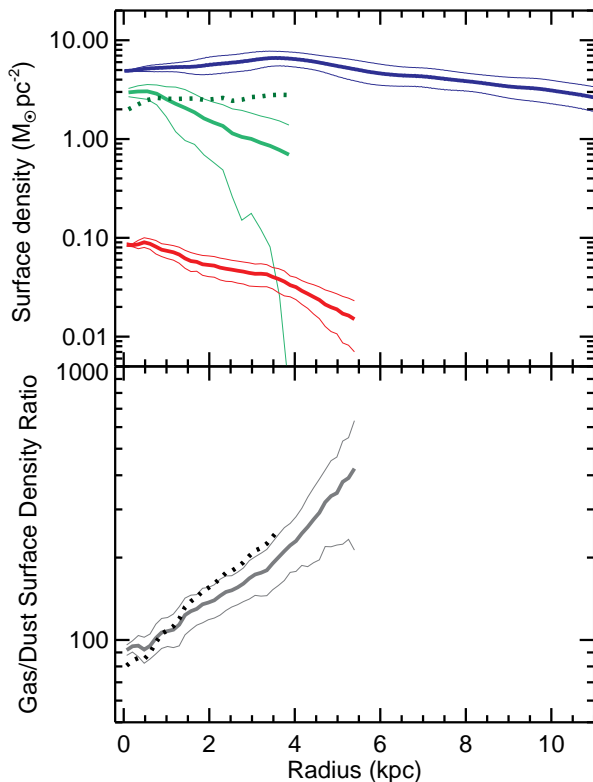
To compare the molecular, atomic, and dust surface densities, we first measured the radial profiles of the surface densities as well as the gas-to-dust ratios. First, all data were convolved with kernels that match the PSFs to that of the  $160\ \mu\text{m}$  data before radial profiles were extracted. The gas-to-dust ratio was calculated on a pixel-by-pixel basis from images regridded to match the astrometry of the dust surface density images. We then measured means, standard deviations, and uncertainties in mean values within elliptical annuli with widths along the major axes that were equal to 2 pixels (or 9 arcsec in the dust and gas-to-dust ratio data, 14.6 arcsec in the molecular gas data, and 2 arcsec in the atomic gas data). This method for setting the annuli widths was used to avoid problems with noise caused by having too few pixels fall within given annuli, but the resulting annuli are small enough that the data, which have a PSF with a FWHM of 38 arcsec, will be Nyquist-sampled. Pixels where CO or HI line emission was not detected were set to 0 in those data. The ratio of the axes in the elliptical annuli were set to account for the inclination of the galaxy ( $62.9^\circ$ ; de Blok et al. 2008).

Figure 7 shows the radial profiles of the HI,  $\text{H}_2$ , and dust surface densities. Two versions of the  $\text{H}_2$  surface densities are shown. The values shown with a solid line were calculated using a constant  $X_{CO}$ , and the values shown with the dotted line were calculated using the formula for  $X_{CO}$  given in Equation 9. For simplicity, we

will refer to the former as the constant  $X_{CO}$  molecular gas surface density and the latter as the variable  $X_{CO}$  molecular gas surface density. Although the standard deviation in the CO  $J=(3-2)$  radial profiles approaches the same level as the mean values at large radii, the uncertainties in the mean values are no wider than the thicknesses of these lines. Hence, the mean values are very well defined even though significant variance may be seen in CO intensities at specific radii.

The figure shows that most of the mass in the interstellar medium of this galaxy is traced by the HI emission, a result also obtained by Thornley & Wilson (1995). The HI surface density is relatively flat; it increases slightly towards 4 kpc and then declines gradually beyond that radius. The constant  $X_{CO}$  molecular gas surface density decreases exponentially with radius. The scale length of the constant  $X_{CO}$  molecular gas radial profile is  $2.32 \pm 0.07$  kpc. The variable  $X_{CO}$  molecular gas surface density, however, is so close to flat that it is not possible to accurately fit an exponential function to the profile. The dust surface density, like the constant  $X_{CO}$  molecular gas surface density, decreases with radius. Its radial profile has an exponential scale length of  $3.16 \pm 0.10$  kpc. If we applied an additional correction for radiation field strength in  $X_{CO}$ , then this would increase the molecular gas surface density in regions with high radiation field intensities, which would correspond to regions in the centre of NGC 2403 with higher dust temperatures shown in Figure 4. Therefore, the molecular gas surface density radial profile would fall in between those of the constant  $X_{CO}$  and variable  $X_{CO}$  molecular gas surface densities plotted in Figure 7.

Of particular interest is how the radial profiles of the molecular gas changes when the abundance-dependent correction is introduced. If the variable  $X_{CO}$  molecular gas surface density is an accurate depiction of the true surface density, then it implies that  $\sim 25\%$  of the ISM at large radii is comprised of molecular gas. If true, this would contradict the typical depiction of how the ratio of molecular to atomic gas varies within spiral galaxies, with the centres of galaxies being dominated by molecular gas and the outer discs being dominated by atomic gas (Wong & Blitz 2002;



**Figure 7.** Radial profiles of the HI surface density (solid blue line, top panel), H<sub>2</sub> surface density (green lines, top panel), and dust surface density (solid red line, top panel) as well as the total (molecular and atomic) gas-to-dust surface density ratio (bottom panel) plotted up to 10 kpc, which is equivalent to the edge of the optical disc. For the H<sub>2</sub> and gas/dust ratios, the solid lines are for quantities calculated using a constant  $X_{CO}$  and the dotted lines are for quantities calculated using a value of  $X_{CO}$  that depends on  $12+\log(O/H)$ . The standard deviations of the data are plotted as thinner lines around all radial profiles except for the H<sub>2</sub> surface density and gas-to-dust ratios calculated with a variable  $X_{CO}$ , which have standard deviations that are similar to the equivalent quantities calculated with the constant  $X_{CO}$ . The uncertainties in the mean values are generally smaller than the thicknesses of these lines. The H<sub>2</sub> and dust radial profiles are truncated at the maximum radii where the quantities could be reliably measured along the major axis (4 and 5.5 kpc, respectively). The gas-to-dust ratio calculated using the constant  $X_{CO}$  is also truncated at the maximum radius at which the dust surface densities could be measured. The gas-to-dust ratio calculated using the variable  $X_{CO}$  is truncated at 4 kpc to show how the change in  $X_{CO}$  affects this ratio; beyond this radius, the radial profile merges back into the other gas-to-dust radial profile.

Bigiel et al. 2008, e.g.). However, these prior results rely upon the assumption that  $X_{CO}$  is constant. This issue should be examined further using radial profile data for other galaxies and using deeper CO data to determine if molecular gas surface densities calculated using an  $X_{CO}$  that depends on metallicity are found to still be significant contributors to the total gas surface density at larger radii and in other galaxies. If found to be true, then we need to more carefully consider how to convert CO intensities into molecular gas surface densities and possibly revise the standard depiction of the structure of the ISM in spiral galaxies.

The bottom panel of Figure 7 shows two radial profiles of the gas-to-dust ratio based on the two different molecular gas surface

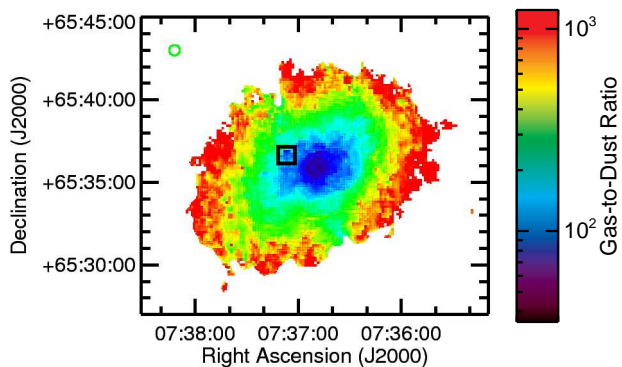


**Figure 8.** Image of the gas-to-dust surface density ratio in NGC 2403. The image is 21 arcmin  $\times$  18 arcmin with north up and east to the left. Only pixels where the dust mass was measured are shown. The molecular gas surface densities were calculated assuming that  $X_{CO}$  is constant, although the functionality of  $X_{CO}$  does not strongly affect the appearance of this figure. The green circle in the upper left corner shows the 38 arcsec FWHM of the PSF, which is equivalent to the PSF of the 160  $\mu$ m data. The black square indicates the location of VS 44.

densities used in this analysis. Both radial profiles increase relatively smoothly with radius. Because the atomic gas is the largest component of the ISM, differing assumptions in  $X_{CO}$  have only a minor impact on the radial profiles within the shown range. Within a kpc of the center, the ratio is seen to drop to  $\sim 100$ . For comparison, the expected gas-to-dust ratio in the Milky Way near the Earth, based either on the measurement of the depletion of metals from the gaseous phase of the ISM or on the ratio of gas column densities to optical extinction, is 100-200 (Krügel 2003; Whittet 2003; Li 2004; Krügel 2008). As we indicated above, the dust masses that we have calculated are low compared to more sophisticated models of dust emission, so it is unlikely that we have underestimated the central gas-to-dust ratio. Instead, it is quite possible that the ISM in the centre of NGC 2403 is relatively dust-rich. The gas-to-dust ratio reaches a value of  $\sim 150$  at about 2 kpc. At radii of 5.5 kpc, which is the limit of where we can accurately measure the radial profile of the dust in this galaxy, the ratio reaches  $\sim 400$ .

Figure 8 shows the total gas-to-dust ratio for all pixels in which we measured dust masses. To make this image, the data were convolved with kernels that match the PSFs to that of the 160  $\mu$ m data (which has a FWHM of 38 arcsec). This image shows that the gas-to-dust ratio appears to increase monotonically with radius. Most structures visible in Figures 1 and 3 are not at all visible. Even VS 44, which has a very high surface brightness in many of the images shown in Figure 2, appears indistinct compared to other locations at similar radii. The only features that are not radially symmetric are the streaks at the northwest and southeast edge of the mapped data that are a result of the latent image artefacts in the 70  $\mu$ m data. The results from Figure 8 suggest that the gas-to-dust ratio is primarily dependent on radius and that it does not vary significantly between diffuse and star-forming regions.

Figure 8 is only useful as a qualitative demonstration of how the gas-to-dust ratio depends primarily on radius and not on gas surface density. As an additional quantitative demonstration of this phenomenon, we used techniques similar to what were used by Bendo et al. (2008) in their comparisons of PAH 8, 24, and 160  $\mu$ m emission. We used the HI, H<sub>2</sub> (calculated using a constant  $X_{CO}$ ),

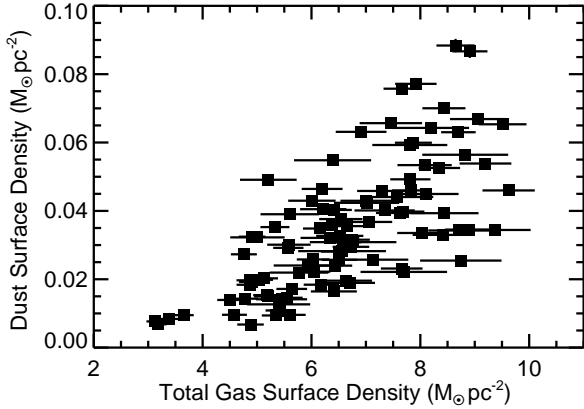
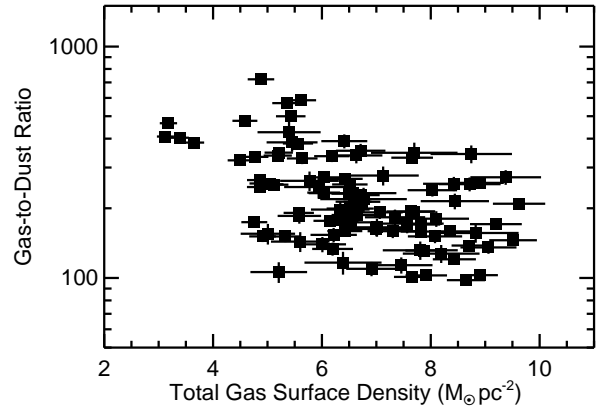


**Figure 9.** The dust surface density versus the total (atomic and molecular) gas surface density for 45 arcsec<sup>2</sup> regions in NGC 2403. The data were extracted from images that had all been convolved with kernels that match the PSFs to that of the 160  $\mu\text{m}$  data. Only regions within 5.5 kpc (the limit at which the dust masses can be reliably measured) and with S/N ratios  $> 5$  were used. Uncertainties in the ordinate are generally smaller than the symbols in this plot and the next two plots. See the text in Section 5 for a description of how these surface densities were extracted.

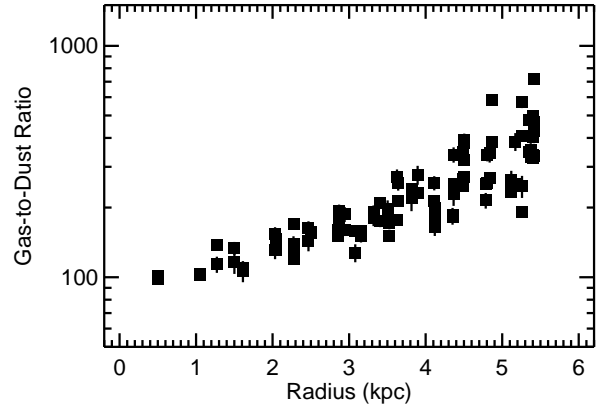
and dust surface density maps that were used to create Figure 8. We rebinned these data into 45 arcsec pixels. This pixel size was selected because it is an integer multiple of the pixel size used for the MIPS data that is also close to the 38 arcsec FWHM of the 160  $\mu\text{m}$  data. We then extracted the surface densities from each 45 arcsec<sup>2</sup> region in the data. Because the H I is the dominant component of the ISM in this galaxy, the choice of  $X_{CO}$  in this analysis has a minor impact on the results.

Figure 9 shows that the total gas density is related to the total dust density for these 45 arcsec square regions, but the relation exhibits significant scatter. For a given gas surface density, the dust surface density could vary by a factor of 5. Figure 10 shows how the gas-to-dust ratio varies with gas surface density. This is an alternative form for plotting the data in Figure 9; if a one-to-one relation existed between the gas and dust surface densities, then the relation in Figure 10 should have a slope of 0 and exhibit little scatter. The data in Figure 10 actually exhibit a negative slope ( $-79 \pm 13 (\text{M}_{\odot} \text{pc}^{-2})^{-1}$ ) and significant scatter. Figure 11 shows how the gas-to-dust ratio varies with galactocentric radius for these 45 arcsec<sup>2</sup> regions. The relation here shows much less scatter; gas-to-dust ratios at a given radius may vary by a factor of 2 or less.

Using the Spearman’s rank correlation coefficient, which is a non-parametric correlation coefficient that is useful when dealing with data that may exhibit non-linear (i.e. exponential) relations, we can demonstrate that the relation in Figure 11 is more significant than the relation in Figure 9. For reference, perfectly correlated data would have a coefficient of 1, and uncorrelated data would have a coefficient of 0. The correlation coefficient for the relation between gas and dust surface densities in Figure 9 is 0.73, which would imply a good correlation. However, the correlation coefficient for the relation between the gas-to-dust ratio and radius is 0.91. These results demonstrate that the relation between the gas-to-dust ratio and radius places stronger constraints on dust surface densities than the total gas surface density by itself. Moreover, this quantitative approach confirms that the absence of visible structure in Figure 8 is not simply a consequence of the poor resolution of the data. Instead,



**Figure 10.** The gas-to-dust ratio versus the total (atomic and molecular) surface density for 45 arcsec<sup>2</sup> regions in NGC 2403. See the caption for Figure 9 for additional information.



**Figure 11.** The gas-to-dust ratio versus radius for 45 arcsec<sup>2</sup> regions in NGC 2403. This can be considered an alternate version of the bottom panel in Figure 7. See the caption for Figure 9 for additional information.

it is a result of the gas-to-dust ratio being primarily dependent on radius. However, it is always possible that local variations in the gas-to-dust ratio will be visible in higher-resolution data.

The most obvious driver for this gradient in the gas-to-dust ratio is the decrease in metallicity with radius that has been observed previously (see Section 2.6). The gas-to-dust ratio is naturally expected to increase as abundances decrease simply because fewer constituents of dust should be present in the ISM. Gas-to-dust ratios significantly higher than the local Milky Way value of  $\sim 150$  have been measured in many dwarf galaxies with low metallicities (e.g. Lisenfeld & Ferrara 1998; Walter et al. 2007), and globally-integrated measurements of gas-to-dust ratios are correlated with globally-integrated  $12+\log(\text{O}/\text{H})$  or metallicity measurements (e.g. Issa et al. 1990; James et al. 2002; Draine et al. 2007; Hirashita et al. 2008). Moreover, Lisenfeld & Ferrara (1998) and Muñoz-Mateos et al. (2009) have found linear relations between oxygen abundances and dust-to-gas ratios in nearby galaxies. Although the dust-to-gas ratios typically decrease faster than the oxy-

gen abundances in these relations, the slopes are still on the order of 1.

As stated in 2.6, the typical gradient in  $12+\log(\text{O}/\text{H})$  that has been measured in NGC 2403 is  $-0.084 \pm 0.009 \text{ dex kpc}^{-1}$ . For comparison, we measured the gradient in the logarithm of the dust-to-gas ratio ( $d\log(\sigma_{\text{dust}}/\sigma_{\text{gas}})/dr$ ) to be  $-0.097 \pm 0.002 \text{ dex kpc}^{-1}$  for NGC 2403. These gradients are so close that it implies that the dust-to-gas ratio is primarily dependent on metallicity. Alternatively, when we calculated  $12+\log(\text{O}/\text{H})$  as a function of radius, we found the relation between  $12+\log(\text{O}/\text{H})$  and  $d\log(\sigma_{\text{dust}}/\sigma_{\text{gas}})/dr$  had a slope of  $0.86 \pm 0.02$ . This slope is less than 1, which is consistent with the results obtained by Lisenfeld & Ferrara (1998) and Muñoz-Mateos et al. (2009), but it is so close to 1 that it implies a linear relationship between the oxygen abundance and the dust-to-gas ratio. Variations in the ratio of oxygen to the other constituents of dust could explain the difference in the gradients. Garnett et al. (1999), for example, has shown that C/O increases systematically with O/H within this galaxy as well as within M 101, and since carbon is a primary constituent of dust,  $d\log(\sigma_{\text{dust}}/\sigma_{\text{gas}})/dr$  would be expected to be steeper than the gradient in  $12+\log(\text{O}/\text{H})$ . Additional comparisons between radially-averaged dust-to-gas ratios and  $12+\log(\text{O}/\text{H})$  using all of the data from SINGS, THINGS, and the JCMT NGLS would be appropriate to determine whether similar results are typically obtained for all spiral galaxies.

Some researchers (e.g. Neininger et al. 1996; Israel 1997) have suggested that  $X_{\text{CO}}$  for any galaxy can be determined in a two step process. First the gas-to-dust ratio is measured in a region dominated by atomic gas. Second, that ratio is applied to a region that contains CO and dust emission to determine how much molecular gas should be present, thus giving  $X_{\text{CO}}$ . However, the results here show that the application of this method to spiral galaxies must be performed cautiously. The first problem is that this method assumes that the gas-to-dust ratio is constant, whereas we have demonstrated that it varies with radius. The second problem is that, as explained in Section 4,  $X_{\text{CO}}$  may depend on metallicity, and metallicity will vary with radius in most nearby galaxies. Despite these problems, it may still be possible to derive  $X_{\text{CO}}$  within subsections of galaxies by dividing the galaxies into elliptical annuli where both the metallicity and the gas-to-dust ratio will remain constant. If regions free of molecular gas but containing detectable atomic gas and dust emission can be identified within the individual annuli, then those locations can be used to measure the gas-to-dust ratio at specific radii. Those regions can then be used to infer the gas-to-dust ratio for locations at similar radii that contain detectable CO emission to determine how much gas should be present and therefore what  $X_{\text{CO}}$  is needed to account for all of the gas. This will then lead to a measure of  $X_{\text{CO}}$  as a function of radius. Unfortunately, it is not possible to apply this method to the data used here. To perform this analysis correctly, we would need to work with data where the PSFs matches the 40 arcsec resolution of the 160  $\mu\text{m}$  data. When the CO data are matched to the 160  $\mu\text{m}$  PSF, the area within radii of 4 kpc (the region in which CO  $J=(3-2)$  emission is detected along the major axis) contains almost no CO-free regions for comparison to regions where CO is detected.

It is possible that the observations here may have missed the presence of very cold dust (dust with temperatures  $< 15 \text{ K}$ ) that may not contribute strongly to the 70 and 160  $\mu\text{m}$  bands but that may constitute the bulk of the dust mass at larger radii. As argued in Appendix A, it is unclear in cases where submillimetre emission has been observed in excess of the  $\sim 20 \text{ K}$  thermal dust models fit to the 70 and 160  $\mu\text{m}$  data whether this excess originates from

large masses of  $< 15 \text{ K}$  dust or very low masses of dust with enhanced submillimetre emissivities. Results from previous analyses have suggested that estimates of the dust mass based on the 70 and 160  $\mu\text{m}$  wave bands should be well within an order of magnitude of the expected dust mass (Lisenfeld et al. 2002; Dumke et al. 2004; Regan et al. 2004; Bendo et al. 2006; Draine et al. 2007). Based on these previous results, we expect the gas-to-dust ratio shown in Figure 7 to be accurate and to not be strongly affected by large masses of dust not traced by the 70 and 160  $\mu\text{m}$  bands. It is nonetheless possible that the radial increase in our measured gas-to-dust ratio could be linked to an increase in the relative fraction of  $< 15 \text{ K}$  dust with radius, but to properly determine this will require both submillimetre measurements of the dust emission and models of this dust emission that incorporate accurate submillimetre emissivities based on laboratory and theoretical results.

## 6 COMPARISON OF PAH, CO $J=(3-2)$ , AND HI EMISSION

As we are interested in re-examining the empirical correlation between CO and PAH emission found by Regan et al. (2006) using the higher-sensitivity HARP-B data, and as they used radial profiles to show this correlation, we will first look at the radial profiles for the CO  $J=(3-2)$  intensity and PAH 8  $\mu\text{m}$  surface brightness. Since Regan et al. (2006) used the CO intensities for their analysis instead of converting the CO intensities to molecular gas surface densities, we will compare the PAH 8  $\mu\text{m}$  surface brightnesses directly to the CO  $J=(3-2)$  intensities.

The radial profiles for the HI intensity, CO  $J=(3-2)$  intensity, and PAH 8  $\mu\text{m}$  surface brightness are shown in Figure 12. All data were convolved with kernels that match the PSFs to that of the CO  $J=(3-2)$  data (which has a FWHM of 14.5 arcsec) before radial profiles were extracted. The techniques used for extracting these radial profiles are the same as those used in Section 5, although we only used data in which the CO emission was detected to calculate the CO  $J=(3-2)$ /PAH 8  $\mu\text{m}$  ratio. The width of the elliptical annuli along the major axis in the CO  $J=(3-2)$  and CO  $J=(3-2)$ /PAH 8  $\mu\text{m}$  ratio that we used was still equivalent to 2 pixels (or 14.6 arcsec), which does not result in Nyquist-sampled radial profiles. However, using narrower elliptical profiles results in excessive noise because of the low numbers of pixels falling within the elliptical annuli. While the standard deviations in the CO  $J=(3-2)$  and PAH 8  $\mu\text{m}$  radial profiles are sometimes greater than the plotted radial means, just as was the case with the CO radial profiles in Figure 7, the standard deviation does not equate to the the uncertainties in the means. The uncertainties in the means are actually smaller than the thickness of the lines in Figure 12 except for the ratio of the CO  $J=(3-2)$  intensity to PAH 8  $\mu\text{m}$  surface brightness. In effect, we can actually measure the means to a relatively high precision, but we still see significant variance in the data.

In the top panel of the figure, we can see that the radial profile of the CO  $J=(3-2)$  and PAH 8  $\mu\text{m}$  emission are similar to each other. In contrast, the HI radial profile is much broader than either the CO  $J=(3-2)$  or PAH 8  $\mu\text{m}$  radial profiles. Given the dissimilarity between the PAH 8  $\mu\text{m}$  and HI radial profiles as well as the dramatic differences between the appearance of the 8  $\mu\text{m}$  and HI images in Figures 1 and 2, we can conclude that the PAH 8  $\mu\text{m}$  emission is not associated with HI in this galaxy. We will not discuss the HI further but instead focus on the comparison between the CO  $J=(3-2)$  and PAH 8  $\mu\text{m}$ .

The CO  $J=(3-2)$  and PAH 8  $\mu\text{m}$  radial profiles not only appear



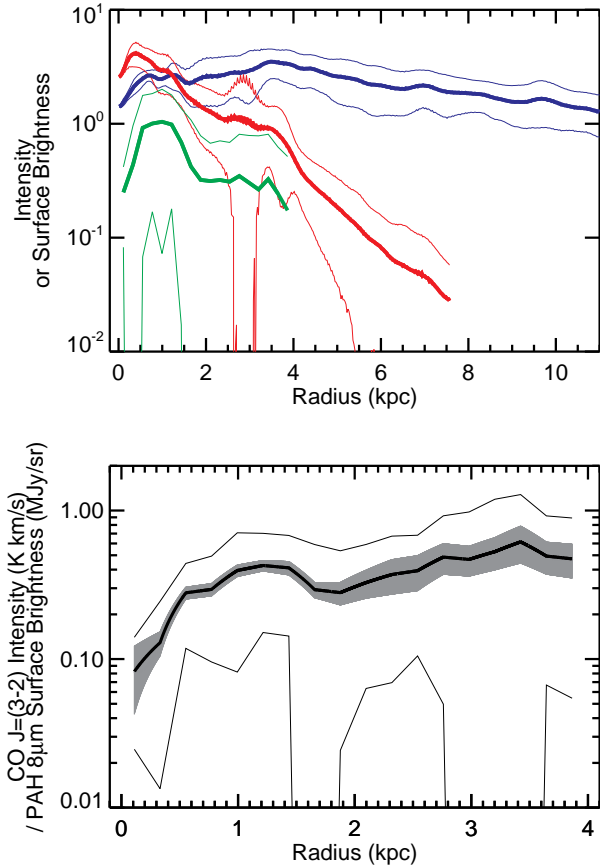


**Figure 12.** Radial profiles of the HI intensity in  $\text{Jy beam}^{-1} \text{ km s}^{-1}$  (blue line, top panel), CO  $J=(3-2)$  intensity in  $\text{K km s}^{-1}$  (green line, top panel), and PAH  $8 \mu\text{m}$  surface brightness in  $\text{MJy sr}^{-1}$  (red line, top panel) as well as the ratio of CO  $J=(3-2)$  intensity to PAH  $8 \mu\text{m}$  surface brightness (black line, bottom panel) plotted up to 10 kpc, which is equivalent to the edge of the optical disc. All data were convolved with kernels that match the PSF of the CO  $J=(3-2)$  data (which has a FWHM of 14.5 arcsec) before radial profiles were extracted. The standard deviations of the data are plotted as thinner lines around all radial profiles. The uncertainties in the mean values are generally smaller than the thicknesses of these lines except in the case of the CO  $J=(3-2)$ /PAH  $8 \mu\text{m}$  emission ratio, where the uncertainty is shown as a shaded grey region. The CO  $J=(3-2)$  and PAH  $8 \mu\text{m}$  radial profiles are truncated at the radii beyond which the quantities could be reliably measured on the major axis. The ratio in the bottom panel is also truncated at the maximum radius where CO  $J=(3-2)$  intensities could be reliably measured.

superficially similar but also have similar exponential scale lengths. Between 0.5 kpc and 4 kpc, the CO  $J=(3-2)$  radial profile has an exponential scale length of  $2.0 \pm 0.2$  kpc. The PAH  $8 \mu\text{m}$  emission (in the convolved data) has a scale length of  $1.99 \pm 0.04$  kpc over the same range. The plot of the ratio of the two in the bottom panel of Figure 12 shows that the ratio between 0.5 and 4 kpc has a gradient of  $0.070 \pm 0.017$   $(\text{K km s}^{-1}) (\text{MJy sr}^{-1})^{-1} \text{ kpc}^{-1}$ , but the mean value for the ratio stays between  $\sim 0.25$  and  $\sim 0.6$  at radii between 0.5 and 4 kpc. However, while the mean in the CO  $J=(3-2)$ /PAH  $8 \mu\text{m}$  ratio remains relatively constant over this range of radii, the high standard deviation shows that the ratio fluctuates greatly at any given radius. The implications of this are discussed further below.

The CO  $J=(3-2)$ /PAH  $8 \mu\text{m}$  emission ratio decreases sharply in the nucleus of the galaxy. This drop in the ratio corresponds to drops in the surface brightness in both wave bands. The drop in the ratio may be in part related to variations in the gas-to-dust ratio described in Section 5, but that would not explain why the ratio appears close to constant at larger radii, nor would it explain why the CO and PAH emission also drops near the nucleus. We can exclude the possibility that currently-ongoing intense nuclear star formation may be inhibiting PAH emission (either through destroying PAHs or through changing their ionization state) and ionizing gas in the centre of the galaxy; both H $\alpha$  (e.g. Drissen et al. 1999) and  $24 \mu\text{m}$  images Bendo et al. (e.g. 2008) show that the nucleus is relatively quiescent compared to other star-forming regions which do have PAH  $8 \mu\text{m}$  and CO  $J=(3-2)$  counterparts. Because this galaxy is classified as having an HII nucleus (e.g. Ho et al. 1997), and no other study indicates the presence of an AGN in NGC 2403, we can also exclude the possibility that an AGN could be responsible for the decrease in PAH and CO  $J=(3-2)$  emission in the nucleus.

The reason for the decrease in PAH  $8 \mu\text{m}$  and CO  $J=(3-2)$  in the nucleus of the galaxy may be explained by the simple fact that, like many other late-type spiral galaxies, the ISM is clumpy and that this galaxy does not contain centrally-concentrated gas and dust emission (e.g. Bendo et al. 2007). The clumpiness of the ISM would also explain why the standard deviations in the PAH  $8 \mu\text{m}$  and CO  $J=(3-2)$  radial profiles in the top panel of Figure 12 are very large. The CO  $J=(3-2)$ /PAH  $8 \mu\text{m}$  emission ratio may decrease towards the centre simply because the two wave bands may not be correlated on sub-kpc scales. The comparison of the PAH  $8 \mu\text{m}$  and CO  $J=(3-2)$  images in Section 3 visually demonstrates this; some structures in the PAH  $8 \mu\text{m}$  image were not as bright as those in the CO  $J=(3-2)$  image and vice versa. Additionally, the high standard deviation in the radial profile of the CO  $J=(3-2)$ /PAH  $8 \mu\text{m}$  ratio implies that the PAH  $8 \mu\text{m}$  and CO emission are not well-correlated at any given radius.

For an explicit quantitative analysis to demonstrate that PAH  $8 \mu\text{m}$  and CO  $J=(3-2)$  emission does not trace the same structures on small spatial scales, we could not use the same binning procedure used to compare the dust surface density versus total gas surface density in Section 5. The gaps between detected structures in the CO  $J=(3-2)$  images made the binned data difficult to interpret. As an alternative, we used surface brightnesses measured in a series of discrete regions. We selected 25 regions with the highest intensity in the CO  $J=(3-2)$  image and the 25 regions with the highest surface brightnesses in the PAH  $8 \mu\text{m}$  image (convolved with a kernel to match its PSF to the PSF of the CO  $J=(3-2)$  data). These regions were defined using the coordinate system of the CO  $J=(3-2)$  data; each region is 3 pixels  $\times$  3 pixels in the CO  $J=(3-2)$  data ( $21.8 \text{ arcsec} \times 21.8 \text{ arcsec}$  or  $330 \text{ pc} \times 330 \text{ pc}$ ). Some of the regions overlap, and some regions are not centered on peak-like emission but instead selected to attempt to cover resolved structures. The regions were also selected to avoid locations that may have been severely affected by foreground stars. Any locations that were affected by foreground stars in the PAH  $8 \mu\text{m}$  data were blanked out in both data sets before surface brightnesses were extracted. These regions are shown in Figure 13. The extracted surface brightnesses are plotted in Figure 14.

The relation between CO  $J=(3-2)$  and PAH  $8 \mu\text{m}$  surface brightness differs between the two sets of data, demonstrating the presence of regions bright in one band but not the other. The regions selected in the PAH  $8 \mu\text{m}$  data exhibit virtually no correlation; the Pearson's correlation coefficient for these data is 0.07. The regions selected in the CO  $J=(3-2)$  data do exhibit a weak correlation; the

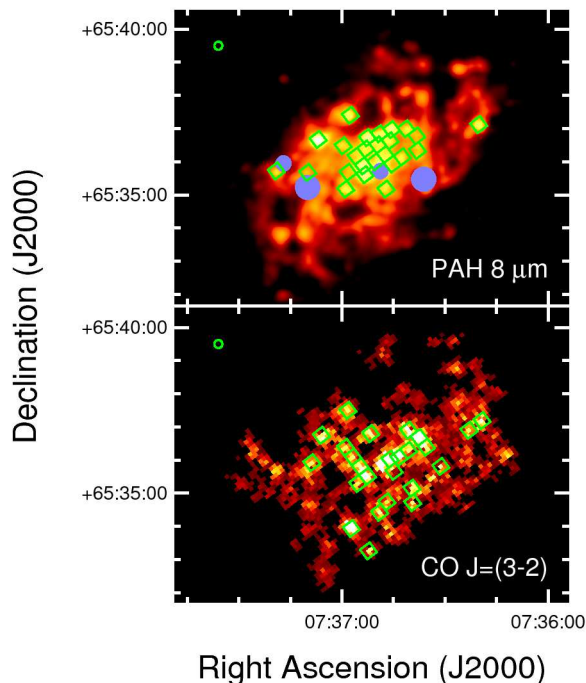


**Figure 13.** Images of the PAH  $8\ \mu\text{m}$  and CO  $J=(3-2)$  emission for the central  $12 \times 9$  arcmin region in NGC 2403 with green squares overlaid to show where intensities or surface brightnesses were measured. The regions selected by their CO  $J=(3-2)$  intensities are shown in the CO  $J=(3-2)$  image, and the regions selected by their PAH  $8\ \mu\text{m}$  surface brightnesses are shown in the PAH  $8\ \mu\text{m}$  image. See the text for details on the region selection. The PAH  $8\ \mu\text{m}$  image has been convolved with a kernel to match its PSF to that of the CO  $J=(3-2)$  image. The green circles in the upper left corner of each image show the 14.5 arcsec FWHM of the CO  $J=(3-2)$  PSF. Blue regions in the PAH  $8\ \mu\text{m}$  image show regions strongly affected by stars that were excluded from the analysis in both wave bands.

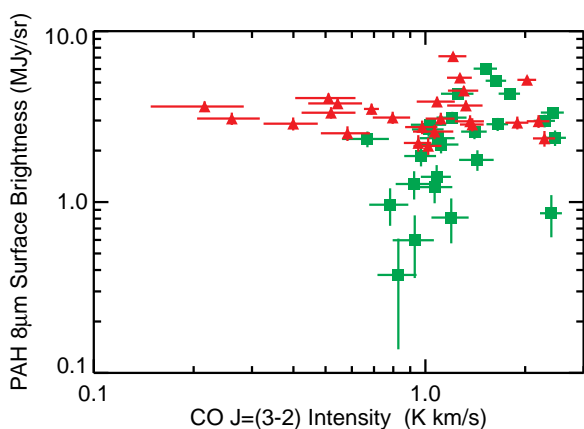


**Figure 14.** Comparison of the CO  $J=(3-2)$  intensity and PAH  $8\ \mu\text{m}$  surface brightness for the regions shown in Figure 13. The regions selected by their CO  $J=(3-2)$  intensity are shown as green squares. The regions selected by their PAH  $8\ \mu\text{m}$  surface brightness are shown as red triangles.

data have a Pearson’s correlation coefficient of 0.32. Given that the square of the Pearson’s correlation coefficient indicates the fraction of variation in one variable that can be accounted for by a best fit line between the data, we find that, in the CO-selected data, only  $\sim 10\%$  of the variation observed in one band can be accounted for by a relation with the other band. In the PAH  $8\ \mu\text{m}$ -selected data,  $< 1\%$  of the variation in one band can be accounted for by a relation with the other band. We therefore conclude that, at best, PAH  $8\ \mu\text{m}$  emission is only weakly correlated with CO  $J=(3-2)$  emission on scales of 330 pc within this galaxy, even though the radial profiles have very similar scale lengths.

We can reject a couple of possible scenarios that would explain why the radial profiles for the PAH  $\mu\text{m}$  and CO  $J=(3-2)$  emission should match even while the emission mechanisms are not correlated on smaller spatial scales. First of all, PAHs and CO do not share a common origin. PAHs are thought to form in the atmospheres of or outflows from AGB stars or in interstellar shocks (Tielens 2008), while molecular gas is commonly assumed to form on the surfaces of interstellar dust grains (Krügel 2003, 2008). It is also unlikely that the radial profiles are matched through the Schmidt law, which relates star formation to gas surface density (Schmidt 1959; Kennicutt 1998). While star formation is strongly dependent on molecular gas surface densities in subregions within galaxies (Kennicutt et al. 2007; Bigiel et al. 2008; Wilson et al. 2009), PAH emission is not strongly linked to other star formation tracers on sub-kpc scales (e.g. Calzetti et al. 2005, 2007; Thilker et al. 2007; Bendo et al. 2008). Moreover, Bendo et al. (2008) demonstrated that the ratio of PAH  $8\ \mu\text{m}$  emission to  $24\ \mu\text{m}$  emission (which has been shown to be correlated with other star formation tracers) decreases as a function of radius within NGC 2403, and the ratio of PAH  $8\ \mu\text{m}$  emission to other star formation tracers would be expected to vary similarly.

On possible link between PAH and CO emission is possible if molecular cloud formation is triggered in regions with stellar potential wells as suggested by Leroy et al. (2008). The new molecular clouds would produce CO emission. Additionally, the increased starlight in these potential wells (from both the stars originally present in the wells and new stars formed from the molecular clouds) would heat the diffuse ISM. According to the results from Bendo et al. (2008), enhanced PAH emission will be produced by locations where the interstellar radiation field has increased. Therefore, the stellar potential wells that form molecular gas clouds in this scenario would not only enhance CO emission but also enhance PAH emission, thus linking the two on large spatial scales and resulting in radial profiles that appear similar for both wave bands. However, the enhanced PAH emission does not need to occur within the stellar potential wells but could instead occur in regions surrounding the potential wells. Therefore, regions containing molecular gas could exhibit CO emission correlated with PAH emission while regions without molecular gas would exhibit PAH emission that is uncorrelated with CO emission as shown in Figure 14.

It is also possible that both PAH and CO emission are affected by similar excitation mechanisms. As stated above, enhancements in PAH emission may be indicative of increased heating of the diffuse ISM, which could be caused by enhancing star formation activity (although they still declared that PAH emission was not useful for tracing star formation on sub-kpc scales). Similarly, Knapen & Beckman (1996) postulated based on the comparison of CO radial profiles to other star formation tracers that CO could be excited by the cosmic rays from star formation, and cosmic rays tend to diffuse into the ISM as can be seen by the comparisons of

infrared and radio continuum emission performed by Murphy et al. (2006a), Murphy et al. (2006b), and Murphy et al. (2008). Therefore, increases in star formation could enhance both PAH and CO emission on large spatial scales, which would explain why the radial profiles for PAH and CO emission appear to match each other.

It is also possible that the radial profiles of CO  $J=(3-2)$  and PAH  $8\ \mu\text{m}$  emission are similar simply by coincidence. The radial profiles of both normalized by the total gas surface density are expected to decrease with radius, although for different reasons. Perhaps the multiplicative factors that relate the slope of the CO  $J=(3-2)$  radial profile to that of total gas surface density just happen to match those factors that relate the PAH  $8\ \mu\text{m}$  radial profile to that for total gas surface density, at least in this galaxy and the ones studied by Regan et al. (2006). A more extensive investigation using the whole of the JCMT NGLS sample could potentially reveal galaxies where the PAH  $8\ \mu\text{m}$  and CO  $J=(3-2)$  radial profiles are not similar (i.e. where the radial profiles do not have similar exponential scale lengths). If a sufficient number of such galaxies can be identified, then it would indicate that what was found here was merely a coincidence.

## 7 CONCLUSIONS

We find that the dust surface density depends on the total (atomic and molecular) gas surface density and on radius. The gas-to-dust ratio varies from  $\sim 100$  in the nucleus to  $\sim 400$  at 5.5 kpc, which is the limit at which the dust surface densities can be detected. The logarithm of the slope for the gas-to-dust ratio ( $d\log(\sigma_{\text{dust}}/\sigma_{\text{gas}})/dr$ ), which is  $0.097 \pm 0.002\ \text{dex kpc}^{-1}$ , is very close to the slope in  $12+\log(\text{O}/\text{H})$ , which is usually reported as between  $-0.07$  to  $-0.09\ \text{dex kpc}^{-1}$ . This implies that the gas-to-dust ratio is strongly dependent on metallicity. Additional abundance variations, such as variations in the C/O ratio, could explain the small disparity between  $d\log(\sigma_{\text{dust}}/\sigma_{\text{gas}})/dr$  and  $12+\log(\text{O}/\text{H})$ . Aside from these strong radial variations in the gas-to-dust ratio, the ratio does not appear to vary within the galaxy.

We also find that the PAH  $8\ \mu\text{m}$  and CO  $J=(3-2)$  radial profiles have statistically identical scale lengths. On spatial scales of 220 pc, however, PAH  $8\ \mu\text{m}$  and CO  $J=(3-2)$  emission are uncorrelated. We propose two mechanisms that could link the PAH emission with star formation. First, the CO emission may appear associated with PAH emission if molecular cloud formation is triggered by stellar potential wells. The stars in these potential wells would enhance the radiation field that heats the diffuse ISM, which would enhance PAH emission. Thus, the PAH emission would appear associated with CO emission on large scales but not on small scales. Second, the two wave bands may be related through different excitation mechanisms that are linked through star formation and that affect the ISM on large areas. While PAH emission does not trace star formation on sub-kpc scales, it is expected to be enhanced by increases in the interstellar radiation field that accompany enhanced star formation. Meanwhile, CO emission could be enhanced by the increase in cosmic rays that accompanies enhanced star formation. Thus, radially-averaged PAH and CO emission would both be linked through star formation, even though PAH and CO emission may not be spatially correlated on sub-kpc scales. However, we also do not rule out the possibility that they may just coincidentally have radial profiles with similar scale lengths.

This paper is only a first look at the gas-to-dust ratio and the relation between PAH and CO emission within the JCMT NGLS sample. The SINGS, THINGS, and JCMT NGLS samples were all

selected to contain many of the same galaxies. The subset of galaxies found in all three samples can be used for an extended comparison of dust, molecular gas, and atomic gas surface densities and for comparisons of PAH to CO emission. Moreover, the gradients in the gas-to-dust ratio could then be compared to abundance gradients to examine the relation between the two further.

## ACKNOWLEDGMENTS

We thank the reviewer for his/her comments on this paper. The James Clerk Maxwell Telescope is operated by The Joint Astronomy Centre on behalf of the Science and Technology Facilities Council of the United Kingdom, the Netherlands Organisation for Scientific Research, and the National Research Council of Canada. G.J.B. and D.L.C. were funded by STFC. The research of J.I. and C.D.W. is supported by grants from NSERC (Canada). A.U. has been supported through a Post Doctoral Research Assistantship from the UK Science & Technology Facilities Council. Travel support for B.E.W. and T.W. was supplied by the National Research Council (Canada). This research has made use of the NASA/IPAC Extragalactic Database (NED) which is operated by the Jet Propulsion Laboratory, California Institute of Technology, under contract with the National Aeronautics and Space Administration.

## APPENDIX A: DISCUSSION ON DUST NOT TRACED BY THE MIPS DATA

It is entirely possible that the 70 and 160  $\mu\text{m}$  bands may have missed significant masses of very cold dust (dust with temperatures  $< 15\ \text{K}$ ) within this galaxy. However, it is unclear whether such dust is present.

Many surveys working with *Spitzer* and submillimetre data have not found evidence for very cold dust. The best examples are the results from Dale et al. (2005) and Draine et al. (2007), who worked with *Spitzer* and submillimetre data for 17 spiral and S0 galaxies in the SINGS sample and found no submillimetre emission in excess of what was predicted by dust models that did not include  $< 15\ \text{K}$  dust. Unfortunately, the quality of the submillimetre data used in these studies were quite variable, so it may not have been feasible for Dale et al. (2005) and Draine et al. (2007) to detect submillimetre emission in excess of what is expected from  $> 15\ \text{K}$  dust within most galaxies. A few groups using very high signal-to-noise submillimetre data with ISO or *Spitzer* data have conclusively demonstrated the presence of emission at wavelengths  $> 850\ \mu\text{m}$  in excess of what is expected from  $\sim 20\ \text{K}$  dust within the Milky Way Galaxy (Reach et al. 1995; Finkbeiner et al. 1999), NGC 4631 (Dumke et al. 2004; Bendo et al. 2006), NGC 3310 (Zhu et al. 2009), and a few nearby dwarf galaxies (Lisenfeld et al. 2002; Galliano et al. 2003, 2005). While Galliano et al. (2003) and Galliano et al. (2005) have suggested that this represents emission from a high mass of dust at 5-10 K, most other authors have rejected this explanation because it leads to implausibly low gas-to-dust ratios. Alternatively, the submillimetre emissivity of dust may be enhanced above the  $\lambda^{-2}$  emissivity law commonly used in many dust models (e.g. Li & Draine 2001). Such dust would include grains with exotic shapes, such as fractal dust grains, which would have relatively high submillimetre emissivities relative to their absorption cross sections (Reach et al. 1995; Dumke et al. 2004; Bendo et al. 2006); dust in which resonances from impurities in the dust grains enhances the submillimetre emissivity (Reach et al.

1995; Bendo et al. 2006); or grains with shallow dust emissivities ( $\kappa_{\nu} \propto \lambda^{-\beta}$ , with  $\beta < 2$ ) that would only be visible at submillimetre wavelengths (Finkbeiner et al. 1999; Lisenfeld et al. 2002; Zhu et al. 2009). Additionally, laboratory studies (Agladze et al. 1996; Mennella et al. 1998; Boudet et al. 2005) and at least one theoretical study (Meny et al. 2007) have shown that dust grains exhibit a broad range of emissivities at these wavelength and that submillimetre dust emissivities can be strongly enhanced above the  $\lambda^{-2}$  emissivity function that is commonly used in astronomical research. In all of these alternate scenarios, the mass of the dust that produces the excess submillimetre emission is relatively low, and most of the dust mass should be traced by dust that dominates the SED at  $< 450 \mu\text{m}$ . Moreover, the results from Lisenfeld et al. (2002), Dumke et al. (2004), Regan et al. (2004), Bendo et al. (2006), and Draine et al. (2007) have demonstrated that, based on the total gas content and expected gas-to-dust ratios for nearby galaxies, most of the dust mass in nearby galaxies can be accounted for by  $\gtrsim 15$  K dust emitting at  $\geq 450 \mu\text{m}$ .

It is always possible that newer  $> 160 \mu\text{m}$  data from either the *Herschel* Space Observatory or SCUBA2 on the JCMT along with improved dust models could demonstrate that the use of *Spitzer* data alone will lead to significant underestimates of dust masses. However, based on current data and models, the dust masses that we measure using only the *Spitzer* data should provide a reasonably accurate estimate of the dust masses. We should not be severely underestimating the dust masses because we have not accounted for large masses of cold dust emitting  $> 160 \mu\text{m}$ .

## REFERENCES

- Agladze N. I., Sievers A. J., Jones S. A., Burlitch J. M., Beckwith S. V. W., 1996, *ApJ*, 462, 1026
- Barone L. T., Heithausen A., Hüttemeister S., Fritz T., Klein U., 2000, *MNRAS*, 317, 649
- Bendo G. J. et al., 2003, *AJ*, 125, 2361
- Bendo G. J. et al., 2006, *ApJ*, 652, 283
- Bendo G. J. et al., 2007, *MNRAS*, 380, 1313
- Bendo G. J. et al., 2008, *MNRAS*, 389, 629
- Berry D. S., Reinhold K., Jenness T., Economou F., 2007, in Shaw R. A., Hill F., Bell D. J., eds., *ASP Conf. Ser. Vol. 376, Astronomical Data Analysis Software and Systems XVI*. Astron. Soc. Pac., San Francisco, p. 425
- Bigiel F., Leroy A., Walter F., Brinks E., de Blok W. J. G., Madore B., Thornley M. D., 2008, *ApJ*, 136, 2846
- Blitz L., Fukui Y., Kawamura A., Leroy A., Mizuno N., Rosolowsky, E., 2007 in Reipurth B., Jewitt D., Keil K., eds., *Protostars and Planets V*. University of Arizona Press, Tucson, USA, p81
- Bolatto A. D., Leroy A. K., Rosolowsky E., Walter F., Blitz L., 2008, *ApJ*, 686, 948
- Boudet N., Mutschke H., Nayral C., Jäger C., Bernard J.-P., Henning T., Meny C., 2005, *ApJ*, 633, 272
- Bresolin F., Garnett D. R., Kennicutt R. C. Jr., 2004, *ApJ*, 615, 228
- Buckle J. V. et al., 2009, preprint (astro-ph/0907.3610)
- Calzetti D. et al., 2005, *ApJ*, 633, 871
- Calzetti D. et al., 2007, *ApJ*, 666, 870
- Currie M. J., Draper P. W., Berry D. S., Jenness T., Cavanagh B., Economou, F., 2008, in Argyle R. W., Bunclark P. S., Lewis J. R., *ASP Conf. Ser. Vol. 394, Astronomical Data Analysis Software and Systems XVII*. Astron. Soc. Pac., San Francisco, p. 650
- Dale D. A., Helou G., 2002, *ApJ*, 576, 159
- Dale D. A. et al., 2005, *ApJ*, 633, 857
- Dale D. A. et al., 2007, *ApJ*, 655, 863
- de Blok W. J. G., Walter F., Brinks E., Trachternach C., Oh S.-H., Kennicutt R. C. Jr., 2008, *AJ*, 136, 2648
- de Vaucouleurs G., de Vaucouleurs A., Corwin H. G., Buta R. J., Paturel G., Fouque P., 1991, *Third Reference Catalogue of Bright Galaxies*, Springer-Verlag, Berlin
- Devereux N. A., Young J. S., 1990, *ApJ*, 359, 42
- Draine B. T. et al., 2007, *ApJ*, 663, 866
- Drissen L., Roy J.-R., Moffat A. F. J., Shara M. M., 1999, *AJ*, 117, 1249
- Dumke M., Krause M., Wielebinski R., 2004, *A&A*, 414, 475
- Engelbracht C. W. et al., 2004, *ApJS*, 154, 248
- Fazio G. G. et al., 2004, *ApJS*, 154, 10
- Fierro J., Torres-Peimbert S., Peimbert M., 1986, *PASP*, 98, 1032
- Finkbeiner D. P., Davis M., Schlegel D. J., 1999, *ApJ*, 524, 867
- Fraternali F., Cappi M., Sancisi R., Oosterloo T., 2002, *ApJ*, 578, 109
- Freedman W. L. et al., 2001, *ApJ*, 553, 47
- Galliano F., Madden S. C., Jones A. P., Wilson C. D., Bernard J.-P., Le Peintre F., 2003, *A&A*, 407, 159
- Galliano F., Madden S. C., Jones A. P., Wilson C. D., Bernard J.-P., 2005, *A&A*, 434, 867
- Garnett D. R., Shields G. A., Peimbert M., Torres-Peimbert S., Skillman E. D., Dufour R. J., Terlevich E., Terlevich R. J., 1999, *ApJ*, 513, 168
- Garnett D. R., Shields G. A., Skillman E. D., Sagan S. P., Dufour R. J., 1997, *ApJ*, 489, 63
- Gordon K. D. et al., 2005, *PASP*, 117, 50
- Gordon K. D. et al., 2007, *PASP*, 119, 1019
- Gordon K. D., Engelbracht C. W., Rieke G. H., Misselt K. A., Smith J.-D. T., Kennicutt R. C. Jr., 2008, *ApJ*, 682, 336
- Haas M., Klaas U., Bianchi S., 2002, *A&A*, 385, L23
- Helfer T. T., Thornley M. D., Regan M. W., Wong T., Sheth K., Vogel S. N., Blitz L., Bock D. C.-J., 2003, *ApJS*, 145, 259
- Helou G. et al., 2004, *ApJS*, 154, 253
- Hildebrand R. H., 1983, *QJRAS*, 24, 267
- Hirashita H., Kaneda H., Onaka T., Suzuki T., 2008, *PASJ*, 60, S477
- Ho L. C., Filippenko A. V., Sargent W. L. W., 1997, *ApJS*, 112, 315
- Hodge P. W., Kennicutt R. C. Jr., 1983, *AJ*, 88, 296
- Israel F. P., 1997a, *A&A*, 317, 65
- Israel F. P., 1997b, *A&A*, 328, 471
- Israel F. P., 2000, in Combes F., Pineau des Forêts G., eds., *Molecular hydrogen in space*. Cambridge University Press, Cambridge, UK, p296
- Israel F. P., 2005, *A&A*, 438, 855
- Israel F. P., Baas F., Rudy R. J., Skillman E. D., Woodward C. E., 2003, *A&A*, 397, 87
- Issa M. R., MacLaren I., Wolfendale A. W., 1990, *A&A*, 236, 237
- James A., Dunne L., Eales S., Edmunds, M. G., 2002, *MNRAS*, 335, 753
- Kennicutt R. C. Jr., 1998, *ApJ*, 498, 541
- Kennicutt R. C. Jr. et al., 2003, *PASP*, 115, 928
- Kennicutt R. C. Jr. et al., 2007, *ApJ*, 671, 333
- Kessler M. F. et al. 1996, *A&A*, 315, L27
- Knapen J. H., Beckman J. E., 1996, *MNRAS*, 283, 251
- Krist J., 2002, *Tiny Tim/SIRTF User's Guide*, SSC, Pasadena
- Krügel E., 2003, *The Physics of Interstellar Dust*. Institute of Physics Publishing, Bristol, United Kingdom

- Krügel E., 2008, *An Introduction to the Physics of Interstellar Dust*. Taylor & Francis, New York
- Leroy A. K., Walter F., Brinks E., Bigiel F., de Blok W. J. G., Madore B., Thornley M. D., 2008, *AJ*, 136, 2782
- Li A., 2004, in Block D. L., Puerani I., Freeman K. C., Groess R., Block E. K., eds, *Astrophysics and space science library* 319, *Penetrating Bars Through Masks of Cosmic Dust*, Kluwer, Dordrecht, 535
- Li A., Draine B. T., 2001, *ApJ*, 554, 778
- Lisenfeld U., Ferrara A., 1998, *ApJ*, 496, 145
- Lisenfeld U., Israel F. P., Stil J. M., Sievers A., 2002 *A&A*, 382, 860
- Mattila K., Lehtinen K., Lemke D., 1999, *A&A*, 342, 643
- Mauersberger R., Henkel C., Walsh W., Schulz A., 1999, *A&A*, 341, 256
- Mennella V., Brucato J. R., Colangeli L., Palumbo P., Rotundi A., Bussolletti E., 1998, *ApJ*, 496, 1058
- Meny C., Gromov V., Boudet N., Bernard J.-Ph., Paradis D., Nayral C., 2007, *A&A*, 468, 171
- Muñoz-Mateos J. C. et al., 2009, *ApJ*, 701, 1965
- Murphy E. J. et al., 2006a, *ApJ*, 638, 157
- Murphy E. J. et al., 2006b, *ApJ*, 651, L111
- Murphy E. J., Helou G., Kenney J. D. P., Armus L., Braun R., 2008, *ApJ*, 678, 828
- Neininger N., Guelin M., Garcia-Burillo S., Zylka R., Wielebinski R., *A&A*, 310, 725
- Paturel G., Theureau G., Bottinelli L., Gougouenheim L., Coudreau-Durand N., Hallet N., Petit C., 2003, *A&A*, 412, 57
- Perez-Gonzalez P. G. et al., 2006, *ApJ*, 648, 987
- Pilyugin L. S., 2001, *A&A*, 373, 56
- Popescu C. C., Tuffs R. J., Völk H. J., Pierini D., Madore, B. F., 2002, *ApJ*, 567, 221
- Reach W. T. et al., 1995, *ApJ*, 451, 188
- Reach W. T. et al., 2005, *PASP*, 117, 978
- Regan M. W. et al., 2004, *ApJS*, 154, 204
- Regan M. W. et al. 2006, *ApJ*, 652, 1112
- Rieke G. H. et al., 2004, *ApJS*, 154, 25
- Rosolowsky E., Simon J. D., 2008, *ApJ*, 675, 1213
- Schmidt M., 1959, *ApJ*, 129, 243
- SINGS Team, 2007, *User's Guide*, SSC, Pasadena
- Spitzer* Science Center, 2007, *Spitzer Observer's Manual* Version 8.0, SSC, Pasadena
- Stansberry J. A. et al., 2007, *PASP*, 119, 1038
- Strong A. W., Mattox J. R., 1996, *A&A*, 308, L21
- Strong A. W., Moskalenko I. V., Reimer O., Digel S., Diehl R., 2004, *A&A*, 422, L47
- Thilker D. A., Braun R., Walterbos R. A. M., 1998, *A&A*, 332, 429
- Thilker D. A. et al., 2007, *ApJ*, 173, 572
- Thornley M. D., Wilson C. D., 1994, *ApJ*, 421, 458
- Thornley M. D., Wilson C. D., 1995, *ApJ*, 447, 616
- Tielens A. G. G. M., 2008, *ARA&A*, 46, 289
- van Zee L., Salzer J. J., Haynes M. P., O'Donoghue A. A., Balonek, T. J., 1998, *AJ*, 116, 2805
- Véron P., Sauvayre A., 1965, *AnAp*, 28, 698
- Vila-Costas M. B., Edmunds M. G., 1992, *MNRAS* 259, 121
- Walter F. et al., 2007, *ApJ*, 661, 102
- Walter F., Brinks E., de Blok W. J. G., Bigiel F., Kennicutt R. C. Jr., Thornley M. D., Leroy A., *AJ*, 136, 2536
- Werner M. W. et al., 2004, *ApJS*, 154, 1
- Whittet D. C. B., 2003, *Dust in the Galactic Environment*, Second Edition. Institute of Physics Publishing, Bristol, United Kingdom
- Williams J. P., de Geus E. J., Blitz L., 1994, *ApJ*, 428, 693
- Wilson C. D., 1995, *ApJ*, 448, L97
- Wilson C. D., Walker C. E., Thornley M. D., 1997, *ApJ*, 483, 210
- Wilson C. D. et al., 2009, *ApJ*, 693, 1736
- Wong T., Blitz L., 2002, *ApJ*, 569, 157
- Young J. S., Schloerb F. P., Kenney J. D., Lord S. D., 1986, *ApJ*, 384, 443
- Young J. S., Xie S., Kenney J. D. P., Rice W. L., 1989, *ApJS*, 70, 699
- Young L. M., Bendo G. J., Lucero D., 2009, *AJ*, 137, 3053
- Zaritsky D., Kennicutt R. C. Jr., Huchra J. P., 1994, *ApJ*, 420, 87
- Zhu M., Papadopoulos P. P., Xilouris E. M., Kuno N., Lisenfeld U., 2009, preprint (astro-ph/0908.1600)
- Zhu, Y.-N., Wu H., Cao C., Li H.-N., 2008, *ApJ*, 686, 155